












ChemZz I: comparing oxygen and iron abundance patterns in the Milky Way, the Local Group, and Cosmic Noon

Stephanie Monty¹   ¹★ Allison L. Strom^{2,3,4}  Thomas M. Stanton⁵  Martyna Chruślińska^{6,7} 
 Fergus Cullen⁵  Chiaki Kobayashi⁸  Tjitske Starkenburg^{2,3,4}  Souradeep Bhattacharya⁸ 
 Jason L. Sanders⁹  and Mark Gieles^{10,11} 

¹*Institute of Astronomy, University of Cambridge, Madingley Road, Cambridge CB3 0HA, UK*

²*Department of Physics and Astronomy, Northwestern University, 2145 Sheridan Road, Evanston, IL 60208, USA*

³*Center for Interdisciplinary Exploration and Research in Astrophysics (CIERA), Northwestern University, 1800 Sherman Avenue, Evanston, IL 60201, USA*

⁴*NSF-Simons AI Institute for the Sky (SkAI), 172 E. Chestnut St, Chicago, IL 60611, USA*

⁵*Institute for Astronomy, University of Edinburgh, Royal Observatory, Edinburgh EH9 3HJ, UK*

⁶*European Southern Observatory, Karl-Schwarzschild-Str 2, D-85748 Garching, Germany*

⁷*Max Planck Institute for Astrophysics, Karl-Schwarzschild-Str 1, D-85748 Garching, Germany*

⁸*Centre for Astrophysics Research, Department of Physics, Astronomy and Mathematics, University of Hertfordshire, Hatfield AL10 9AB, UK*

⁹*Department of Physics and Astronomy, University College London, London WC1E 6BT, UK*

¹⁰*ICREA, Pg. Lluís Companys 23, E-08010 Barcelona, Spain*

¹¹*Institut de Ciències del Cosmos (ICCUB), Universitat de Barcelona (IEEC-UB), Martí i Franquès 1, E-08028 Barcelona, Spain*

Accepted 2025 July 16. Received 2025 July 16; in original form 2025 April 11

ABSTRACT

Our understanding of the chemical evolution of galaxies has advanced through measurements from both distant galaxies across redshift, and our own Milky Way (MW). To form a comprehensive picture, it is essential to unify these constraints, placing them on a common scale and parlance and to understand their systematic differences. In this study, we homogenize oxygen and iron measurements from star-forming galaxies at Cosmic Noon ($z \sim 2-3$) with resolved stellar abundances from the Local Group. The MW is divided into four components, assuming the outer halo is dominated by debris from the Gaia-Sausage-Enceladus (GSE) progenitor. After converting all abundances to a common solar scale, we identify clear α - and iron-enhancement trends with mass in the $z \sim 2-3$ galaxies and find good agreement between these galaxies and the MW high- α disc in [O/Fe] versus [Fe/H]. We also find excellent agreement between the [O/Fe] trends seen in the MW high- and low- α discs with O-abundances seen in old and young planetary nebulae in M 31 respectively, supporting the existence of α -bimodality in the inner regions of M 31. Finally, we use globular cluster ages to project the MW and GSE back in time to $z \sim 3$ and find that their estimated mass, oxygen and iron abundances are strikingly consistent with the mass–metallicity relation of star-forming galaxies at $z \sim 3$. In the future, increased transparency around the choice of solar scale and abundance methodology will make combining chemical abundances easier – contributing to a complete picture of the chemical evolution of all galaxies.

Key words: stars: abundances – Galaxy: abundances – galaxies: abundances – galaxies: evolution – galaxies: high-redshift.

1 INTRODUCTION

Understanding the emergence and growth of galaxies and determining our own galaxy’s place in the larger picture, is a major driver for both the fields of extragalactic and Galactic astronomy. To build a complete picture will require marrying knowledge gained from extragalactic studies with discoveries made through Galactic Archaeology (Freeman & Bland-Hawthorn 2002). As the number of increasingly more distant galaxies continue to grow via the *James Webb Space Telescope* (JWST, e.g. GNz-11 at $z \sim 11$, GHZ2 at $z \sim 12.3$, JADES-GS-z14-0 at $z \sim 14$ and MoM-z14 at $z \sim 14.4$; Bunker et al. 2023; Carniani et al. 2025; Castellano et al. 2024;

Naidu et al. 2025), and thanks to the ongoing efforts of large surveys using ground-based spectrographs at $z \sim 2-3$ (e.g. the K-band Multi Object Spectrograph KMOS^{3D} survey, the Sydney-AAO Multi-object Integral-field spectrograph SAMI galaxy survey, the Sloan Digital Sky Survey Mapping Nearby Galaxies at APO SDSS-MANGA survey, the Middle Ages Galaxy Properties with Integral Field Spectroscopy MAGPI survey, the Keck Baryonic Structure Survey KBSS, VANDELS, and the MOSFIRE Deep Evolution Field MOSDEF program; Rudie et al. 2012; Steidel et al. 2014; Bryant et al. 2015; Bundy et al. 2015; Kriek et al. 2015; Wisnioski et al. 2015; McLure et al. 2018; Foster et al. 2021), our understanding of the physics of galaxy formation and evolution is rapidly evolving.

In parallel to this, our understanding of the formation history of the Milky Way (MW) is continuing to increase thanks, in-part, to the *Gaia* mission making 6D phase space information possible

* E-mail: smonty@nmsu.edu

for billions of MW stars (Gaia Collaboration 2016, 2018, 2023), and dedicated spectroscopic surveys charting the chemical evolution of our Galaxy (e.g. the Gaia-European Southern Observatory survey Gaia-ESO, Large Sky Area Multi-Object Fiber Spectroscopic Telescope LAMOST survey, Apache Point Observatory Galactic Evolution Experiment APOGEE, and GALactic Archaeology with HERMES GALAH survey; Cui et al. 2012; Gilmore et al. 2012; Abdurro'uf et al. 2022; Buder et al. 2025). Finally, promising results from chemodynamics of planetary nebulae (PNe; Bhattacharya et al. 2019a, b, 2021, 2022; Arnaboldi et al. 2022) and early *JWST* results in the Andromeda Galaxy (M 31; Nidever et al. 2024) have opened the door to high precision modelling of our most massive galactic neighbour. Given the rapid development of these three areas of galactic research, the time is now to consolidate what we know about each in the context of *global* galaxy evolution.

Placing the MW in the context of other galaxies is no easy task, exemplified by the ongoing debate as to the nature of ‘MW analogues’ in both observations (e.g. selecting analogues based on structural properties and/or star formation histories; Licquia & Newman 2015; Fraser-McKelvie, Merrifield & Aragón-Salamanca 2019; Boardman et al. 2020; Tan et al. 2024) and simulations (e.g. selecting analogues based on total halo mass and/or resemblance to the Local Group, Kobayashi & Nakasato 2011; Wetzel et al. 2016; Grand et al. 2021). While the overall structure of the MW may be well understood – two disc-like components with distinct vertical and radial scale lengths, an inner spheroid or bulge, a diffuse outer halo, bar and spiral arms (Bland-Hawthorn & Gerhard 2016, for a recent review) – important details, and the origin of each, is still the subject of debate (e.g. the length and pattern speed of the bar and transient nature of the spiral arms; see Hunt & Vasiliev 2025).

In addition to the MW components having distinct spatial (and velocity) distributions, they also show unique chemical distributions indicative of different star formation histories – providing critical clues as to the origin and emergence of each (see Helmi 2020; Deason & Belokurov 2024, for recent reviews of the chemodynamics and formation history of different components). Beyond different metallicity distribution functions found across the inner and outer halo (Gilmore & Wyse 1985; Gilmore, Wyse & Jones 1995; Carollo et al. 2007; Youakim et al. 2020), thick and thin disc (Hayden et al. 2014, 2015; Sharma et al. 2019) and the bulge (Ness et al. 2013; Johnson et al. 2014; Ness & Freeman 2016; Lucey et al. 2021; Ardernd-Arentsen et al. 2024), distinctions also exist between the different MW components in α -element abundances, (elements associated with the α -process e.g. O, Mg, Si, Ca; Burbidge et al. 1957; Kobayashi, Karakas & Lugaro 2020b). This is perhaps most obvious in the α -rich inner, and α -poor outer halo (Wallerstein 1962; Venn et al. 2004; Nissen & Schuster 2010; McKenzie et al. 2024) and the high- α , vertically thick and low- α , vertically thin disc (Fuhrmann 1998; Prochaska et al. 2000; Bensby, Feltzing & Lundström 2003; Reddy, Lambert & Allende Prieto 2006; Bensby, Feltzing & Oey 2014; Hayden et al. 2015), where decades of work deriving abundances from stellar spectra has revealed clear distinctions between the coupled components.

The unique SFHs of each component, implied by the chemical distinctions, have since been confirmed through stellar ages, with the ancient halo (both inner and outer) and high- α disc being significantly older than the low- α disc (Sharma, Hayden & Bland-Hawthorn 2021; Xiang & Rix 2022; Queiroz et al. 2023). Despite a strong legacy of study of the MW, many open questions remain: when did each disc emerge, and what did the MW look like prior to disc formation?

As the number of galaxies with structural and chemical properties observed at intermediate- and high- z continues to increase, answering these questions through observing increasingly ancient and/or better-resolved MW analogues *and* understanding how common the MW’s evolution is in the context of *all* galaxies, will offer an exciting and complementary approach to continued studies of the MW.

In contrast to the long history of resolved studies in the MW, it has only recently been possible to extract iron abundances of stellar populations directly from spectra of star-forming galaxies (SFGs) that were forming $\gtrsim 10$ Gyr ago (at $z \gtrsim 2$). Measuring the stellar metallicity (a proxy of the iron abundance) requires high signal-to-noise (SNR) in the rest-frame far-ultraviolet (FUV) continuum. Early analyses were based on measurements of FUV absorption indices and were typically restricted to lensed sources (e.g. Rix et al. 2004; Dessauges-Zavadsky et al. 2010) or composite spectra (e.g. Halliday et al. 2008), with few measurements of individual sources (e.g. Sommariva et al. 2012). More recently, Steidel et al. (2016) introduced a more complete methodology wherein the full FUV continuum at $\lambda_{\text{rest}} < 2000$ Å is fit with stellar population synthesis (SPS) models to more robustly constrain the stellar metallicity and iron abundance in comparison to the prior absorption index approach.

A plethora of works have since used this methodology to measure the iron abundances of high- z galaxies with the aim of measuring the stellar mass (M_*)–stellar metallicity (Z_*) relationship (e.g. Cullen et al. 2019; Chartab et al. 2024). Combining iron abundances with oxygen abundances from rest-frame optical spectra has revealed that high- z SFGs have supersolar O/Fe ratios, reflecting the lack of enrichment from Type Ia supernovae (e.g. Topping et al. 2020a, b; Cullen et al. 2021; Kashino et al. 2022; Strom et al. 2022; Stanton et al. 2024). Interestingly, there is preliminary evidence of high- z systems following the same trends as the MW discs in the [O/Fe] versus [Fe/H] space (e.g. Cullen et al. 2021; Kashino et al. 2022), based on overlapping positions of high- z galaxies with the chemical evolution models describing MW stars of Kobayashi et al. (2020b). Recent studies (Arnaboldi et al. 2022; Kobayashi et al. 2023) have also demonstrated that supernova enrichment processes can be similarly probed in emission nebulae, including SFGs both locally (Bhattacharya et al. 2025) and at high- z (Bhattacharya et al. 2025; Rogers et al. 2024; Morishita et al. 2025; Stanton et al. 2025) using O and Ar abundance measurements. In this case, Ar acts as a proxy for Fe based on the contribution of the Fe-peak nucleosynthetic pathway to the production of Ar (Kobayashi et al. 2020b). However, high- z studies of multi-element abundance ratios, such as O/Fe, remain limited by small samples with sufficient SNR to robustly measure Fe, in particular (note that this is changing with *JWST*, where Fe-measurements out to $z > 9$ are possible with SNR > 40 spectra; Ji et al. 2025; Nakane et al. 2024, 2025).

Despite these limitations, many interesting abundance trends are emerging in early galaxies as the number of measurements increases. First, it is becoming apparent that enhanced O/Fe abundances are ubiquitous in SFGs at these redshifts; although independent studies disagree on the typical level of enhancement, all analyses so far find that $\langle [\text{O}/\text{Fe}] \rangle > 0$ with high significance (with the exception of GNz-11, which could be dominated by a massive star cluster, explaining an apparent enhancement in N in conjunction with a depletion in O; Charbonnel et al. 2023; D’Antona et al. 2023; Nakane et al. 2024). These findings are consistent with enrichment dominated by short time-scale core-collapse supernovae at these cosmic epochs (e.g. Tinsley 1979; Matteucci & Greggio 1986; Chruślińska et al. 2024) and could be the result of high specific star-formation rates

Table 1. Overview of the abundance samples used in this study, highlighting the survey or object of focus and the relevant reference. In the case of M 31, we adopt the binned values for the inner PNe found at radial distances of between 3–14 kpc. As defined previously, ‘SFG’ refers to star forming galaxies.

Survey/Object	Redshift ($\langle z \rangle$)	Iron (N)	Oxygen (N)	Reference(s)	Notes
Local Group					
MW, GSE	0	78691, 1557	78691, 1557	GALAH DR3: Buder et al. (2021)	Stellar abundances
M 31	0	10	10	Bhattacharya et al. (2022)	PNe
GCs	0	16	16	Carretta et al. (2010)	Stellar abundances
LMC	0	17	17	Pompéia et al. (2008)	Stellar abundances
		99	99	Van der Swaelmen et al. (2013)	Stellar abundances
SMC	0	165	165	Mucciarelli et al. (2023)	Stellar abundances
Sagittarius, M 54	0	27, 76	27, 76	Carretta et al. (2010)	Stellar abundances
Cosmic Noon					
NIRVANDELS	3.5	17	34	Cullen et al. (2021), Stanton et al. (2024)	Individual SFGs
	3.5	4	4	Cullen et al. (2021), Stanton et al. (2024)	Stacked SFGs
KBSS	2.4	1	1	Steidel et al. (2016)	Stacked SFGs
	2.3	–	–	Strom et al. (2022)	MZR locus
LATIS	2.5	1	1	Chartab et al. (2024)	Stacked SFGs

($sSFR = SFR/M_*$). Secondly, there is emerging evidence for mass-dependent sequences in $[O/Fe]$ versus $[Fe/H]$ space suggesting lower star-formation efficiencies and possibly greater outflow efficiencies in lower mass galaxies (e.g. Sybilka et al. 2018; Vincenzo, Kobayashi & Taylor 2018; Chartab et al. 2024; Stanton et al. 2024; Velichko et al. 2024); this trend is consistent with local observations of dwarf galaxies (e.g. Tolstoy, Hill & Tosi 2009).

With the overarching goal of exploring the evolution of galaxies across cosmic time through their chemical abundances and placing the MW and Local Group in the context of what is currently known at Cosmic Noon ($z \sim 2-3$), we assembled the ChemZz¹ collaboration of chemical abundance enthusiasts. In this study, we present our first attempt to homogenize extragalactic and Galactic chemical abundance data sets, revealing similarities and differences between the two. In this first paper, we focus only on the evolution of oxygen as a function of iron, as it is well-measured in both environments. To do this, we explore abundances in populations of old, evolved stars in the MW and the Local Group assuming that they act as proxies of the young stellar populations observed in our $z \sim 2-3$ sample.

The paper is organized as follows, we begin by introducing the ‘Toolkit’ in Section 2, where we attempt to bring readers from both the extragalactic and Galactic community ‘up to speed’ on field-specific terminology and methodology. In Section 3, we discuss our compilation of MW and Local Group abundances, define our selection of different MW structural components, describe how we bring all of the abundances on to a common scale (that of Kobayashi et al. 2020b) and include a discussion of systematics. In Section 4, we discuss our sample of Cosmic Noon abundance measurements and again include a discussion of systematic uncertainties. All data sets used in this study are summarised in Table 1. In Section 5, we present our homogenized data set of abundances in chemical space, interpret trends and compare and contrast abundances seen in our Cosmic Noon and Local galaxy populations. In Section 6, we explore incorporating ages for MW field stars and globular clusters (GCs) in an effort to place the MW at $z \sim 3$ or a look-back time of 11.7 Gyr. We conclude by highlighting a first attempt to assess the location of the MW on the $z \sim 3$ mass–metallicity relation for SFGs. Finally, we provide a discussion of next steps and a ‘wish list’ for both the extragalactic and galactic communities

to consider as we pursue a complete picture of galaxy evolution together.

2 THE ‘TOOLKIT’

In this section, we introduce the terminology and concepts referenced throughout the remainder of the paper, with the goal of placing readers from both the Galactic and extragalactic communities on equal footing. We begin by defining ‘metallicity’ and ‘abundance,’ transition to discussing abundance scales (including our preferred scale), and finish by reviewing the connection between the position of systems in abundance space and galactic chemical evolution (GCE).

2.1 Terminology

There are many ways of referring to the enrichment of heavy elements (beyond He) in astrophysical systems. The vocabulary used in a given setting depends on the object(s) being studied, the method(s) employed to study them, and convention – i.e. the choice is partly physical and partly practical. The most basic (if deceptively simple) concept is that of ‘metallicity’ Z , which refers to the *mass fraction* of all elements heavier than helium; Z is often reported relative to the solar metallicity, $Z_{\odot} \sim 0.014$ (Asplund et al. 2009), and may specifically refer to the metallicity of stars (Z_*) or the metallicity in the gas (Z_{gas} or, sometimes, Z_{neb} ; see Maiolino & Mannucci 2019, for a more detailed description). Note that the value of Z_{\odot} may vary slightly across different fields in astrophysics and is revised periodically as our knowledge of the Sun has improved (e.g. most recently in Asplund, Amarsi & Grevesse 2021).

However, in *practice*, astronomers do not measure Z observationally but instead measure the amount of specific elements. So, it is more common to refer to the ‘abundance’ of these elements, defined as $A(X) = 12 + \log_{10}(X/H)$, where X/H stands in for the *number* (or number density) of atoms of some element relative to hydrogen and the abundance of hydrogen is defined as being equal to 12. Abundances are also frequently reported relative to solar abundances, usually using the so-called bracket notation, so that $[X/H] = \log_{10}(X/H) - \log_{10}(X/H)_{\odot}$; both $A(X)$ and square bracket notation were introduced by Helfer, Wallerstein & Greenstein (1959). The relative abundance of different heavy elements can be reported using the same notation, so the ratio of oxygen (O) to iron (Fe) might be written as $[O/Fe] = \log_{10}(O/Fe) - \log_{10}(O/Fe)_{\odot}$. For a recent

¹Upper case ‘Z’ in this context refers to the total abundance of metals (see Section 2, while lower case ‘z’ refers to redshift.

review of abundance determination techniques and applications in stellar spectra, see the work by Nissen & Gustafsson (2018).

As a shorthand, many studies use the word ‘metallicity’ when referring to $A(X)$; for example, this is very common in studies of SFGs, where oxygen is usually the easiest (and sometimes only) elemental abundance that can be measured. This substitution has the practical benefit of allowing direct comparison with theoretical models (which often use Z) but also has the obvious drawback of implicitly assuming that the system under consideration has a *solar-scaled* abundance pattern. However, $[X/H] = -1$ only corresponds to $Z = 0.1 Z_{\odot}$ if *all* elements have $[X/H] = -1$. Yet, in many cases, the relative abundance of different elements is not solar (i.e. $[X/H]$ is not equal for all elements or $[X_2/X_1]$ is non-zero), and these differences can have important physical implications (see Section 2.3). Consequently, eliding the distinction between ‘abundance’ and ‘metallicity’ may introduce confusion and uncertainty unless a study is very clear about their assumptions.

Bearing all of this in mind, in this study we will only use the term ‘metallicity’ when referring to the total iron abundance ($[Fe/H]$) in each system, as is the convention in studies of resolved stellar abundances in the Local Group (see e.g. Venn et al. 2004; Tolstoy et al. 2009; for large abundance compilations). All MW and Local Group abundances used throughout this study (with the exception of M 31) are measured from resolved stellar spectra of individual stars. More specifically, $[Fe/H]$ is determined from absorption features in the stellar spectra associated with different atomic transitions occurring in the stellar atmosphere. Note that $[Fe/H]$ may be derived from measurements of singly-ionized iron or doubly-ionized iron, or an average of the two (again, see Nissen & Gustafsson 2018, for a review of the techniques used to determine stellar abundances). Measurements of metallicity in our high- z sample (often referred to as ‘stellar metallicities’ in that community) are determined using various methods, although most operate on a similar principle to the method used to measure individual stellar metallicities, just for a *population* of stars.

In addition to Fe, we also discuss O throughout this study. As for Fe, $A(O)$ as reported in the various Local Group studies is determined from O absorption lines present in the stellar spectra (again, with the exception of M 31, see Section 3.4). For the Local Group, both $[Fe/H]$ and $A(O)$ (or $[O/H]$) refer to *stellar* enrichment, as the abundances of these elements are determined directly from stellar spectra; the same is true for high- z measurements of $[Fe/H]$. However, in contrast, $A(O)$ in high- z galaxies is measured using emission lines originating from the hot, ionized gas surrounding massive stars in star-forming regions and is often described as the ‘gas-phase metallicity.’ For the sake of clarity and to distinguish it from $A(Fe)$ and $[Fe/H]$, we will not refer to $A(O)$ or $[O/H]$ as ‘metallicity’ in this work, even though it is common parlance in studies of SFGs beyond the Local Group.

2.2 Abundance scales

All of the data sets compiled in this work have chosen to place themselves on a particular solar scale. Despite adopting a common reference object (the Sun), values for the absolute solar abundance of Fe and O can vary from study to study by magnitudes comparable to the abundance uncertainties (e.g. 0.08 dex in the case of O derived using two different treatments of 3D NLTE; Asplund et al. 2009, 2021; Steffen et al. 2015). To compare abundance patterns across our compilation of MW and high- z data, we must first reconcile the various choices of abundance scale and zero point.

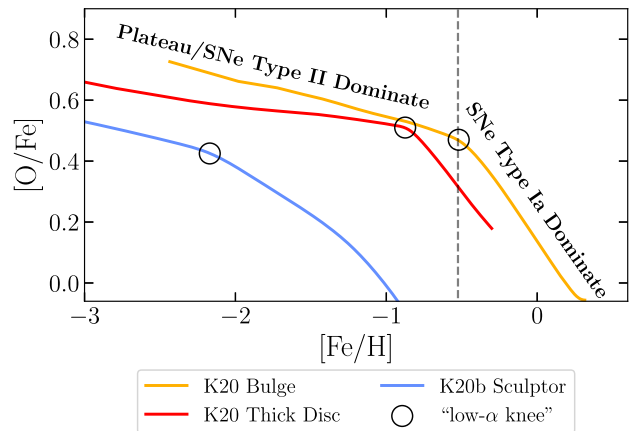


Figure 1. Representation of the ‘Tinsley–Wallerstein’ diagram (Wallerstein 1962; Tinsley 1979), depicting the predicted chemical evolution of three different systems as a result of different star formation histories. Nucleosynthetic sources (driving the evolution) are marked, as well as the location of the ‘low- α ’ knee in the three systems. Predictions for the evolution of the MW bulge and thick disc modelled by Kobayashi et al. (2020b) and the Sculptor dwarf galaxy modelled by Kobayashi, Leung & Nomoto (2020a) are marked in yellow, red, and blue, respectively.

To overcome these differences, we place all of the Fe and O abundances in our compilation on to the solar scale of Kobayashi et al. (2020b, hereafter K20), who in turn adopt $A(Fe)_{\odot} = 7.50$ from Asplund et al. (2009) and $A(O)_{\odot} = 8.76$ from Steffen et al. (2015) for a bulk (proto-)solar metallicity of $Z_{\odot} = 0.0144$; for completeness, Asplund et al. (2009) report a bulk (proto-)solar metallicity of $Z_{\odot} = 0.0142$. Note that we will specify the choice of solar scale used throughout when discussing or plotting $[O/Fe]$ or $[Fe/H]$. For example, values on the ‘K20 scale’ are denoted as $[Fe/H]_{K20}$ and $[O/Fe]_{K20}$.

2.3 The Tinsley–Wallerstein diagram and galactic chemical evolution

To interpret the set of chemical abundances and connect them to galaxy evolution, we use the Tinsley–Wallerstein diagram (Wallerstein 1962; Tinsley 1979). This diagram (depicted in Fig. 1) traces formation time-scales by comparing elements originating from different nucleosynthetic sites. On the y-axis (ordinate), an element (or an average of several elements) associated with the α -process is plotted as a function of metallicity ($[Fe/H]$, see Section 2.1) marked on the x-axis (abscissa). The dominant fusion site for α -elements is inside massive stars (through hydrostatic burning) and through the subsequent core-collapse (explosive burning, in Type II, Ib, and Ic supernova; Woosley & Weaver 1995; Woosley, Heger & Weaver 2002; Kobayashi et al. 2006, 2020b). As a result, the time-scales for α -element production are relatively short, commensurate with the lifetime of massive stars, meaning that elements like O and Mg re-enter the interstellar medium (ISM) on time-scales of 10–100 Myr.

In addition to the α -elements, massive stars also introduce iron into the ISM at early times. This balance of both α -element and iron production produces a plateau in $[O/Fe]$ over a range in metallicity, as seen in Fig. 1 (where we have chosen O as our α -element tracer). After as little as ~ 100 Myr, low-mass stars end their lives as Type Ia supernovae (SNe), synthesizing and releasing Fe-peak elements (e.g. Ti, Cr, Mn, Fe, Ni) into the ISM (Woosley et al. 2002; Kobayashi et al. 2006). Because Type Ia SNe produce Fe but not α -elements, the

overall ratio of $[\alpha/\text{Fe}]$ declines as a function of increasing metallicity. The onset of Type Ia SNe is associated with the appearance of the ‘low- α knee’ in the Tinsley–Wallerstein diagram – providing a timestamp in metallicity for a galaxy’s evolution [though Mason et al. (2024) find that the appearance of a ‘low- α knee’ in simulations is only associated with the onset of Type Ia *if* a galaxy has a steadily declining star-formation rate (SFR), we revisit this later].

Connecting the Tinsley–Wallerstein diagram to galaxy evolution, α -element production and entry into the ISM is sensitive to both the number of massive stars as well as the SFR, or equally, the star formation efficiency (SFE), if the efficiency is assumed to be constant as in the case where $N = 1$ in the Schmidt–Kennicutt star formation law such that $\text{SFR} = \text{SFE} \times M_{\text{gas}}$ (Schmidt 1959; Kennicutt 1998). As a result, galaxies that have high star formation efficiencies, or equally high sSFRs, *and* are continuously forming stars, maintain a plateau in $[\alpha/\text{Fe}]$ to higher values of $[\text{Fe}/\text{H}]$, than galaxies that are less efficient or ‘slow’ at forming stars, even after the onset of Type Ia enrichment. Examples of this are shown in Fig. 1 where the rapid assembly of the MW Bulge (represented with a chemical evolution model in yellow from Kobayashi et al. 2020b) appears distinct from the slow star-formation history (SFH) of the much less massive Sculptor dwarf galaxy (dGal, in blue). The positions of the low- α -knees in these two galaxies are significantly displaced in $[\text{Fe}/\text{H}]$, with SF halting in Sculptor at significantly lower metallicities than the Bulge. The Kobayashi et al. (2020b) model for the MW thick disc is also included in Fig. 1 in red, highlighting another system that experienced efficient star formation.

In summary, the SFH and temporal evolution of a galaxy are reflected in their evolution through the Tinsley–Wallerstein diagram. To derive a SFH from the chemical evolution of a galaxy through the diagram, analytical GCE models are used, with the simplest being the ‘closed-box model.’ In the closed-box model, enriched gas is converted into stars with some global SFE and no loss or gain to the mass budget via outflows or inflows. More modern GCE models (see Matteucci 2021, for a full review) involve more realistic galactic physics (including inflows and outflows, e.g. OMEGA; Côté et al. 2017), bursty star formation (e.g. flexCE; Andrews et al. 2017), stellar migration (e.g. VICE; Johnson et al. 2021) and multiple nucleosynthetic channels tracing both common and rare events (e.g. neutron star mergers, magneto-rotational supernovae, Kobayashi et al. 2020b). Throughout this paper, we will use both observational data and GCE models from K20 to interpret the chemical evolution of the galaxies in our sample.

3 MILKY WAY AND THE LOCAL GROUP

In this section, we describe the selection criteria we apply to the MW field star data and our chemodynamical definitions of the MW structural components, namely: the low- α (thin) and high- α (thick) discs, and the inner and outer halo. We also discuss the data sets we include for MW GCs and Local Group galaxies. The section concludes with a discussion of our efforts to bring the various samples on to a common abundance scale and some systematic uncertainties relevant for studies of resolved stellar abundances.

3.1 GALAH DR3 sample selection

Oxygen abundance measurements of resolved MW field stars are taken from the third data release of the GALactic Archaeology with HERMES (GALAH) survey (De Silva et al. 2015; Buder et al. 2021). GALAH is a medium resolution ($R \sim 28\,000$) spectroscopic survey of 588571 Southern hemisphere stars (81.2 per cent of which are

within 2 kpc of the Sun) conducted using the HERMES spectrograph (Sheinis et al. 2015) and the 2dF fibre positioning system (Lewis et al. 2002) on the 3.9 m Anglo-Australian Telescope. The wavelength coverage (although discontinuous) spans 4713–7887 Å, capturing absorption features associated with 30 unique elements, across four nucleosynthetic channels (α , Fe-peak, s - and r -process). Very broadly, stellar abundances in DR3 are determined using Spectroscopy Made Easy (Valenti & Piskunov 1996; Piskunov & Valenti 2017), a spectrum synthesis code and 1D MARCS model atmospheres (Gustafsson et al. 2008), with the final stellar abundances determined through χ^2 minimisation of the synthetic and observed spectra on an element-by-element basis (see section 3.2 in Buder et al. 2021, for a more detailed discussion). We adopt DR3 for this study, rather than DR4, because the abundances are derived using a standard approach for which the systematics are better understood at present (versus abundances derived using a machine learning approach, as in DR4; Buder et al. 2025).

We choose to adopt GALAH oxygen abundances because they are determined using optical O I absorption lines² and have been corrected to account for deviations from local thermodynamic equilibrium (NLTE corrections) following Amarsi et al. (2020). This is important as NLTE is implicitly assumed as part of the abundance derivations in our Cosmic Noon data set. Unfortunately, O abundances derived from IR spectra from the Apache Point Observatory Galactic Evolution Experiment (APOGEE; Abuduro’uf et al. 2022) have not been NLTE corrected, likely because they are measured from OH molecular lines (Jönsson et al. 2020), so we neglect them in this study. Furthermore, systematic differences are known to exist between O abundances derived from optical spectra with those derived from infrared spectra, complicating efforts to combine data from different surveys (Carrillo et al. 2022).

To construct our catalogue of GALAH DR3 stars, we follow Monty et al. (2024) and the recommendations from GALAH regarding which flagged stars to remove.³ That is, we remove stars with `snr_c3_iraf` < 30, `flag_sp` \neq 0, `flag_fe_h` \neq 0 and `flag_o_fe` \neq 0. To sample the old stellar populations in the MW – which are most analogous to the young, massive stellar populations observed in our Cosmic Noon sample – we select only red giant branch stars in our study, stipulating cuts on the effective temperature ($T_{\text{eff}} \leq 5300$ K) and surface gravity ($\log g \leq 3$). Finally, we require abundance uncertainties of less than 0.2 dex in $[\text{O}/\text{Fe}]$ and $[\text{Fe}/\text{H}]$ to build our clean data set. In total, we retain $\sim 80\,000$ stars from the original DR3 catalogue, with an average $T_{\text{eff}} \sim 4650$ K and $\log g \sim 2$.

3.2 Defining Milky Way components

Under the assumption that the different structural components of the MW emerged at different times, we aim to explore the evolution of each in relation to our Cosmic Noon samples with fixed look back times. To do this, we split the GALAH data into four structural components: the low- α (thin) and high- α (thick) discs and inner and outer halo. Because these components were formed at different times via different channels, they have distinct chemodynamical signatures. Consequently, we can apply various dynamical and chemical cuts to isolate each component, as described below, relying on both historical definitions and recent discoveries.

²Specifically the three O I near-IR lines at 7771.94, 7774.17, and 7775.35 Å.

³https://www.galah-survey.org/dr3/using_the_data/

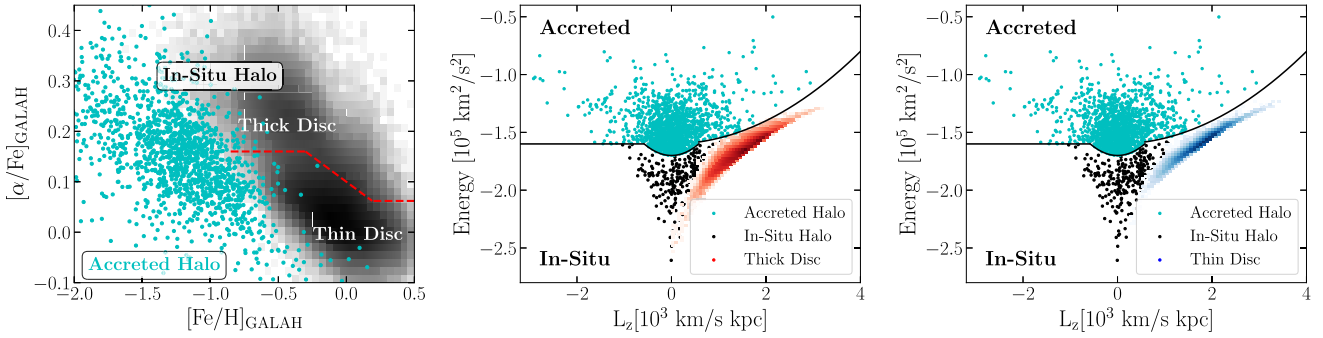


Figure 2. The four MW components from our GALAH sample shown in both chemical and dynamical space. From left to right, the first column shows our definition for the four components in $[\alpha/\text{Fe}]$ versus $[\text{Fe}/\text{H}]$ space. The three *in situ* components are shown in black, while stars from the accreted halo are marked in cyan. Our chemical definition separating the high- α (thick) and low- α (thin) discs is marked in red, following the methodology of Mackereth et al. (2019). The second column shows the location of the accreted (cyan) and *in situ* (black) halo components in energy (E) versus z -component of angular momentum (L_z) separated by the boundary derived in (Belokurov & Kravtsov 2023). The location of the high- α disc is marked in red. The third column repeats what is shown in the second, with the exception that the low- α disc is now shown in blue.

Dynamical properties for the GALAH DR3 stars are taken from the GALAH_DR3_VAC_dynamics_v2 value-added catalogue described in Buder et al. (2022). To calculate E , L_z , and other orbital parameters, Buder et al. (2022) adopt the MW potential from McMillan (2017) implemented within the GALPY galactic dynamics package (Bovy 2015). Buder et al. (2022) adopt a solar radius of 8.21 kpc and orient the Sun 25 pc above the plane, following Jurić et al. (2008). Their total solar velocity of $(U, V, W) = (11.1, 248.27, 7.25) \text{ km s}^{-1}$ in keeping with Schönrich, Binney & Dehnen (2010), after assuming the same circular velocity at the Sun (233.1 km s^{-1}) as McMillan (2017).

3.2.1 *In situ* and accreted halo

The first cut we make to isolate MW components is to define *in situ* and *accreted* stars within the MW. We consider the more spatially compact inner MW halo (also referred to as the high- α halo or ‘Aurora’; Nissen & Schuster 2010; Bonaca et al. 2020; Belokurov & Kravtsov 2022) and the low- α and high- α discs to be the predominant *in situ* components. Before applying chemical cuts, we first split both the GALAH sample into *in situ* and accreted stars based on energy, E and z -component of the angular momentum, L_z . We apply the $E - L_z$ boundary derived in Belokurov & Kravtsov (2023) motivated chemically by a difference in $[\text{Al}/\text{Fe}]$ seen between the inner and outer Galaxy, and assumed to be due to different SFHs – with Al acting as a tracer of massive stellar evolution. As in Monty et al. (2024), the exact $E - L_z$ boundary is adjusted to accommodate the different choice of Galactic potential between Belokurov & Kravtsov (2023) and Buder et al. (2022). After making the adjustment, we require *in situ* stars in GALAH to satisfy the following, where L_z is in units of $(\text{km s}^{-1} \text{ kpc})$ and E is units of (km^2/s^2) :

$$L_z/10^3 < -0.58 : E/10^5 < -1.6$$

$$-0.58 \leq L_z/10^3 < 0.58 : E/10^5 < -1.7 + 0.3L_z^2$$

$$L_z/10^3 > 0.58 : E/10^5 < -1.6 + 0.5L_z^2.$$

After applying cuts in E, L_z , chemical cuts are applied to remove stars with $[\text{Al}/\text{Fe}]_{\text{GALAH}} \leq -0.1$ below metallicities of $[\text{Fe}/\text{H}]_{\text{GALAH}} = -0.6$, as these are likely accreted interlopers. Finally, *in situ* stars are defined as having $[\text{Mg}/\text{Fe}]_{\text{GALAH}} \leq -0.3 \times [\text{Fe}/\text{H}]_{\text{GALAH}}$. Note that the bulk of these cuts are made to exclude

stars below the cut-off in E, L_z that likely belong to the Gaia-Sausage/Enceladus (GSE) dwarf galaxy (Belokurov et al. 2018; Haywood et al. 2018; Helmi et al. 2018) – the likeliest candidate for the last major merger experienced by the MW. We assign stars which sit above the boundary in E, L_z without applying chemical cuts as accreted halo/GSE stars in GALAH. These stars are marked with the cyan points in Fig. 2. The middle and right panel of Fig. 2 show the distributions of the two populations in E, L_z -space, with the black stars belonging to the *in situ* halo and the blue, the accreted halo.

3.2.2 High- α and low- α discs

The origin of the spatial bimodality of the MW low- α (thin) and high- α (thick) discs is still uncertain. Although it is generally accepted that the thick disc is older (supported by its high α -abundance), the source of its increased vertical scale height is debated – e.g. perhaps it arises through dynamical heating via the last major merger (Mackereth et al. 2019) or perhaps it was born with a large vertical velocity dispersion due to turbulent gas (Wisnioski et al. 2015). Additionally, the origin of the light- (α -)element bi-modality between the two discs and its relation to the spatial differences between the discs as well as its prevalence in other galaxies, also remains uncertain (we discuss this further in Section 5.2). Locally (in the solar neighbourhood), it has been suggested that the α -bimodality could be the result of radial migration, potentially related to the growth and deceleration of the MW bar (Schönrich & Binney 2009; Minchev, Chiappini & Martig 2013; Sharma et al. 2021; Zhang et al. 2025). Regardless of its origin, we split the discs primarily based on this α -bi-modality and verify our results using the spatial distributions.

We make two dynamical cuts to select disc stars among our *in situ* sample, namely that $|z_{\text{max}}| < 3 \text{ kpc}$ and $v_\phi \geq 120 \text{ km s}^{-1}$ to ensure that the stars are both (i) confined to the disc of the Galaxy and (ii) display coherent rotation. After these cuts we follow the methodology of Mackereth et al. (2019) to split the high- α and low- α discs based on the evolution of their $[\alpha/\text{Fe}]$ abundance as a function of metallicity. Following Mackereth et al. (2019), we separate the GALAH *in situ* samples visually using their 2D histograms in $[\alpha/\text{Fe}]_{\text{GALAH}}$ versus $[\text{Fe}/\text{H}]_{\text{GALAH}}$ space, adopting the bulk $[\alpha/\text{Fe}]$ values reported by GALAH. To make a clearer distinction between the two disc populations, we also restrict the low- α population to metallicities above $[\text{Fe}/\text{H}] = -0.6$. The separation we adopt is shown as the red

dashed line in Fig. 2, with the two components annotated. The high- α and low- α disc sample distributions in E, L_z -space are also shown in the middle and right panel of Fig. 2 as the red and blue density distributions, respectively. Because we rely primarily on chemical cuts to separate the thick and thin discs, moving forward we refer to these two components solely as the high- α and low- α discs, respectively.

3.2.3 Shifting on to the K20 abundance scale

To shift our GALAH DR3 sample on to our preferred scale (K20), we bring the individual $[\text{O}/\text{Fe}]_{\text{GALAH}}$ and $[\text{Fe}/\text{H}]_{\text{GALAH}}$ measurements back to $A(\text{O})$ and $A(\text{Fe})$ assuming the solar values published in Buder et al. (2021) [$A(\text{O})_{\odot} = 8.77$, $A(\text{Fe})_{\odot} = 7.38$], before applying the K20 $A(\text{O})$ and $A(\text{Fe})$ values. Buder et al. (2021) derive their solar abundance values through measurements of the solar spectrum observed with the same instrumental set-up as the GALAH survey and verify their scale through reproducing solar-like abundance patterns in Sun-like stars in the solar neighbourhood.

3.3 Globular clusters

To supplement our field star population and provide accurate ages for older stars, we consider $[\text{O}/\text{Fe}]$ and $[\text{Fe}/\text{H}]$ abundances for 16 MW GCs from Carretta et al. (2010). Due to their pronounced chemical complexity (see, e.g. Milone & Marino 2022, for a recent review), computing a single mean value of $[\text{O}/\text{Fe}]$, and in some cases $[\text{Fe}/\text{H}]$, for the set of MW GCs is non-trivial; as more and more GCs are being found to host statistically significant spreads in metallicity (see, e.g. Legnardi et al. 2022; McKenzie et al. 2022; Monty et al. 2023a). In the case of $[\text{O}/\text{Fe}]$, a large spread in O driven by the appearance of an O-normal and O-depleted population is an example of one of the multiple anticorrelations found among light elements in nearly all GCs and produced via the CNO cycle and proton capture chain (resulting in an O-depletion in conjunction with an Na-enhancement, Gratton, Sneden & Carretta 2004). Despite this complexity, the mean $[\alpha/\text{Fe}]$ abundances in GCs have been shown to agree with their dynamical origins, with accreted GCs showing lower $[\alpha/\text{Fe}]$ abundances than *in situ* clusters at the same metallicity in agreement with field star classifications and reflecting a difference in SFE between disrupted dwarf galaxies and the MW (Belokurov & Kravtsov 2023, 2024; Monty et al. 2023b, 2024; Ceccarelli et al. 2025).

Under the assumption that the O-normal population of stars in GCs sample the oxygen abundance of their host galaxies at the time of GC formation, we determine $[\text{O}/\text{Fe}]$ and $[\text{Fe}/\text{H}]$ for the 17 GCs in the Carretta et al. (2009) sample *from these stars alone* and shift them on to our preferred scale (K20). The original Carretta et al. (2009) data assumes the solar scale published in Gratton et al. (2003), namely that $A(\text{Fe})_{\odot} = 7.54$ and $A(\text{O})_{\odot} = 8.79$. Therefore, we added these values back to the $[\text{O}/\text{Fe}]_{\text{CAR}}$ and $[\text{Fe}/\text{H}]_{\text{CAR}}$ values published by Carretta et al. (2009) before subtracting the K20 solar $A(\text{O})$ and $A(\text{Fe})$ values. Note also that O I abundances were determined from the two forbidden lines at 6300 and 6363 Å, which are unaffected by NLTE effects (Amarsi, Nissen & Skúladóttir 2019). To determine the abundance of $[\text{O}/\text{Fe}]_{\text{GC}}$ and $[\text{Fe}/\text{H}]_{\text{GC}}$ for each GC, we average only among the first generation stars with $[\text{O}/\text{Fe}]_{\text{CAR}} \geq [\text{O}/\text{Fe}]_{\text{AVE,CAR}} - \sigma[\text{O}/\text{Fe}]_{\text{CAR}}$ (where σ is the standard deviation in this case) and among stars with $T_{\text{eff}} \leq 5300$ K, $\log g \leq 3$, and $[\text{X}/\text{Fe}]$ uncertainty less than 0.2 dex, in keeping with our GALAH sample selection criteria. On average, these cuts result in mean

cluster abundances being driven by stars with $T_{\text{eff}} \sim 4400$ K and $\log g \sim 1.5$.

Following the classifications from Belokurov & Kravtsov (2023), 10/16 GCs in our sample are classified as having formed *in situ* (i.e. alongside the primordial MW) and 6/16 are classified as being accreted (Belokurov & Kravtsov 2024). Of the six accreted GCs, we re-classify NGC 288 as an *in situ* cluster following the findings of Horta et al. (2020) and Monty et al. (2023b) and assign three of the remaining five GCs as originating in the GSE progenitor galaxy following the classifications of Myeong et al. (2019) and Massari, Koppelman & Helmi (2019). We revisit the implication of these classifications in Section 6.

3.4 Abundances in the Local Group

To explore Cosmic Noon galaxy abundances in the context of as many Local Group galaxies with different stellar masses and SFHs as possible, we also include data from five additional studies. Data for 116 stars in the Large M. Cloud (LMC)⁴ come from the combined studies of Pompéia et al. (2008) and Van der Swaelmen et al. (2013) examining the LMC disc and bar, respectively. Data for 206 stars from the Small M. Cloud (SMC) are taken from Mucciarelli et al. (2023), while data for both the main body of the Sagittarius dwarf galaxy (Sgr, 27 stars) and its nuclear star cluster (M 54, 76 stars) are taken from Carretta et al. (2010).

In addition to local dwarf galaxies, we also include data collected in M 31 from the study of Bhattacharya et al. (2022) by converting their published O and Ar abundances to $[\text{O}/\text{Fe}]_{\text{K20}}$ and $[\text{Fe}/\text{H}]_{\text{K20}}$. Using spectroscopic observations of PNe identified throughout the disc of M 31 (Bhattacharya et al. 2019a, 2021), Bhattacharya et al. (2022) directly measure the abundance of O and Ar from highly ionized emission lines. In addition to abundances, the PNe have ages based on extinction, splitting the sample into old (>4.5 Gyr) and young (<2.5 Gyr) PNe (Bhattacharya et al. 2019b). The O and Ar abundances in both PNe populations were converted to $[\text{O}/\text{Fe}]_{\text{K20}}$ and $[\text{Fe}/\text{H}]_{\text{K20}}$ using GCE models as described in Kobayashi et al. (2023), noting that a substantial fraction of Ar is synthesized alongside Fe in Type Ia SNe (allowing it to act as a tracer of Fe-peak nucleosynthesis). We adopt the binned $[\text{O}/\text{Fe}]_{\text{K20}}$ and $[\text{Fe}/\text{H}]_{\text{K20}}$ data for the two PNe populations in the radial distance range of 3–14 kpc presented in Kobayashi et al. (2023). As stated in Kobayashi et al. (2023), uncertainties on the binned PNe $[\text{O}/\text{Fe}]_{\text{K20}}$ and $[\text{Fe}/\text{H}]_{\text{K20}}$ values are taken from the GCE-transformed measurement error added to the binned standard deviation in quadrature and the bin-width, respectively.

We place all of the additional data sets on to our preferred solar scale thanks to each study explicitly stating their choice of solar scale. That is, $A(\text{O}) = 8.83$, $A(\text{Fe}) = 7.50$ in the case of the LMC (Pompéia et al. 2008; Van der Swaelmen et al. 2013), $A(\text{O}) = 8.76$, $A(\text{Fe}) = 7.50$ in the case of the SMC (Mucciarelli et al. 2023) and the K20 abundances in the case of M 31 (Bhattacharya et al. 2022). Regarding the choice and/or impact of NLTE corrections in each study, as in the case of the GC data, all three studies we consider utilize either one or two forbidden O I lines at 6300 and 6363 Å to measure O, both of which are unaffected by NLTE effects (Amarsi et al. 2019). Given the range of stellar parameters across all three

⁴We acknowledge that the continued use of the name Magellan is both potentially traumatic for Indigenous peoples and factually incorrect, as he did not discover the clouds (de los Reyes, Besla & Oey 2024). We abbreviate the name for the remainder of this paper.

studies ($T_{\text{eff}} \sim 4100$ K, $\log g \sim 1.0$ on average), NLTE corrections to Fe are negligible (Lind, Bergemann & Asplund 2012). Finally, we do not apply NLTE corrections to the M 31 data, as the abundances were determined directly from emission lines.

3.5 Towards a common abundances scale and systematic uncertainties I: Local sample

GALAH is a massive survey, and deriving reliable stellar abundances across such a broad range of stellar parameters and data quality is a mammoth task. To validate the reliability of the GALAH DR3 [O/Fe] values in our selected subset across both metallicity and MW components, we compare the mean GALAH abundances to those derived by Amarsi et al. (2019, hereafter A19). In their study, A19 re-analyse high resolution, high SNR spectra for stars in the high- α and low- α disc and inner and outer halo. Using sophisticated model atmospheres and treatment of NLTE, they derive both 1D NLTE and 3D NLTE abundances for both oxygen and iron across the MW components. Note that although A19 only classify their stars kinematically using the Toomre Diagram (Sandage & Fouts 1987; Carney, Latham & Laird 1988) utilizing the three azimuthal velocity components ($\sqrt{U^2 + W^2}$ versus V), we find good agreement with our more detailed dynamical classifications.

Prior to assessing the agreement between the GALAH abundances and the A19 abundances across different components, we corrected our GALAH sample for temperature-dependent abundance trends. Recently, Kos et al. (2025) identified these trends in the GALAH DR4 sample by selecting star clusters to act as mono-metallic, chemically homogeneous systems (in the case of open clusters) for which the abundances are expected to be consistent across stellar types. They found clear trends with temperature across abundance space in the clusters but were unable to identify the cause of the trends. Although we selected our stars from GALAH DR3, we identified moderate temperature-dependent abundance trends in our low- and high- α samples, weak trends in our sample of inner halo stars and no significant trend in our accreted halo sample. To correct for these temperature trends, we binned each component in metallicity space into 0.3 dex sized bins to approximate near mono-metallic populations and fit the recovered trends with linear functions to flatten the abundances in each bin across temperature. The de-trended [O/Fe]_{K20} abundances were carried forward for all further analysis.

Overall, we find good agreement between the mean trends in the GALAH data (after removing the temperature dependence) and the A19 abundances for each MW structural component. However, after bringing both data sets on to the K20 abundance scale, we still find a 0.25 dex offset in [O/Fe]_{K20,1D,NLTE} between all GALAH and A19 components. We choose only to compare against the 1D results because GALAH DR3 only published 1D NLTE abundances for O and Fe. Given its thorough treatment of abundance uncertainties, we adopt A19 as the ‘ground truth’ and shift the entire GALAH sample down by 0.25 dex in [O/Fe]_{K20}. Both the shifted GALAH data and the A19 data are shown in the left column of Fig. 3. The GALAH data are shown as distributions, with the mean trends marked as dashed lines, while the individual abundance measurements are plotted over top as coloured circles. Note the good agreement across components after shifting to the K20 solar scale and applying a global shift to the GALAH data.

Given the agreement between the mean trends for each component (shown as the dashed line in Fig. 3), we interpret the offset as being associated with oxygen only. Unfortunately, we cannot calibrate the offset directly, because there are only two stars in-common between our GALAH sample and A19. To test if this offset is related to the fact

that our GALAH samples are dominated by giant stars (by design), while the A19 sample is comprised of dwarf stars ($T_{\text{eff,ave}} \sim 5900$ K, $\log g_{\text{ave}} \sim 4.0$), we selected stars within our GALAH components with $T_{\text{eff}} \geq 5500$ K and $\log g \geq 4$ and re-determined the offset between GALAH and Amarsi et al. (2019). The offset decreased slightly to 0.15 dex, when comparing dwarf stars only, but remained present.

The origin of the offset may be related to the choice by GALAH to determine a single, global zero-point for stars across metallicities. That is, they only investigate abundance accuracy and determine a zero-point offset for Sun-like stars at [Fe/H] ~ 0 (Buder et al. 2021), which they then apply to stars across all metallicities.

After comparing the K20-shifted [O/Fe] and [Fe/H] abundances in our GC sample from Carretta et al. (2009) with the A19 high- α disc, *in situ* halo, and accreted halo components (none of our 16 MW GCs are in the low- α disc), we find a ~ 0.15 dex offset between A19 and the GCs in [O/Fe]_{K20} across the different components. Assuming that first generation stars in GCs (see Section 3.3) in each MW structural component should follow the abundance trends found in field stars in that same component (e.g. as shown in Belokurov & Kravtsov 2024; Monty et al. 2020), we again take the A19 data to be the ground truth shift and the entire GC sample *upwards* in [O/Fe]_{K20} by +0.15 dex. The disagreement is on the order twice the average uncertainty in the individual [O/Fe] and [Fe/H] abundance measurements (~ 0.06 and ~ 0.09 , respectively) reported in Carretta et al. (2009).

4 COSMIC NOON GALAXIES

The study of galaxy enrichment beyond $z \sim 0$ has advanced significantly over the last decade, as spectroscopic surveys of $z \sim 2-3$ galaxies have increased in size and quality (e.g. Steidel et al. 2014; Kriek et al. 2015; McLure et al. 2018, among others). These surveys have allowed us to learn not only about bulk metallicity but also abundance patterns in the first few Gyr of cosmic time. In recent years, *JWST* has pushed the frontier of (primarily gas-phase) abundance ratio measurements even further, to $z \sim 8$ and beyond (corresponding to the $\lesssim 650$ Myr after the big bang; e.g. Arellano-Córdova et al. 2022).

To assemble a representative superset of abundance measurements for SFGs in the early Universe, we drew from studies of both individual high- z galaxies and composite spectra as described below. The observable spectra of these galaxies are dominated by light from massive stars and the surrounding star-forming (H II) regions. At non-ionizing rest-UV wavelengths ($\lambda_{\text{rest}} \approx 1000-2000$ Å), we directly observe continuum radiation from O and B stars, imprinted with photospheric absorption, stellar wind features, and interstellar absorption lines; in the rest-optical ($\lambda_{\text{rest}} \approx 3500-7000$ Å), the ionizing radiation from the same stars is reprocessed into hydrogen recombination lines and collisionally-excited forbidden lines of heavier elements such as N, O, Ne, and S. These lines provide detailed information about the physical conditions in the ionized gas in galaxies, including elemental abundances.

It is useful to recall that Fe contributes the majority of the opacity in stellar atmospheres and has the greatest impact on the resulting stellar spectrum, so it is reasonable to assume that $Z_* \approx Z_{\text{Fe}}$. At the same time, the conditions in the gas are closely tied to the abundance of O because oxygen provides some of the most important and efficient cooling pathways, so that $Z_{\text{neb}} \approx Z_{\text{O}}$. To first order, the enrichment of the stars and gas in H II regions is the same, owing to the young ages and short lifetimes of the massive stars responsible for both the rest-UV continuum and the rest-optical emission lines. Consequently, it is common to adopt Z_* as the level of Fe enrichment and Z_{neb} as the

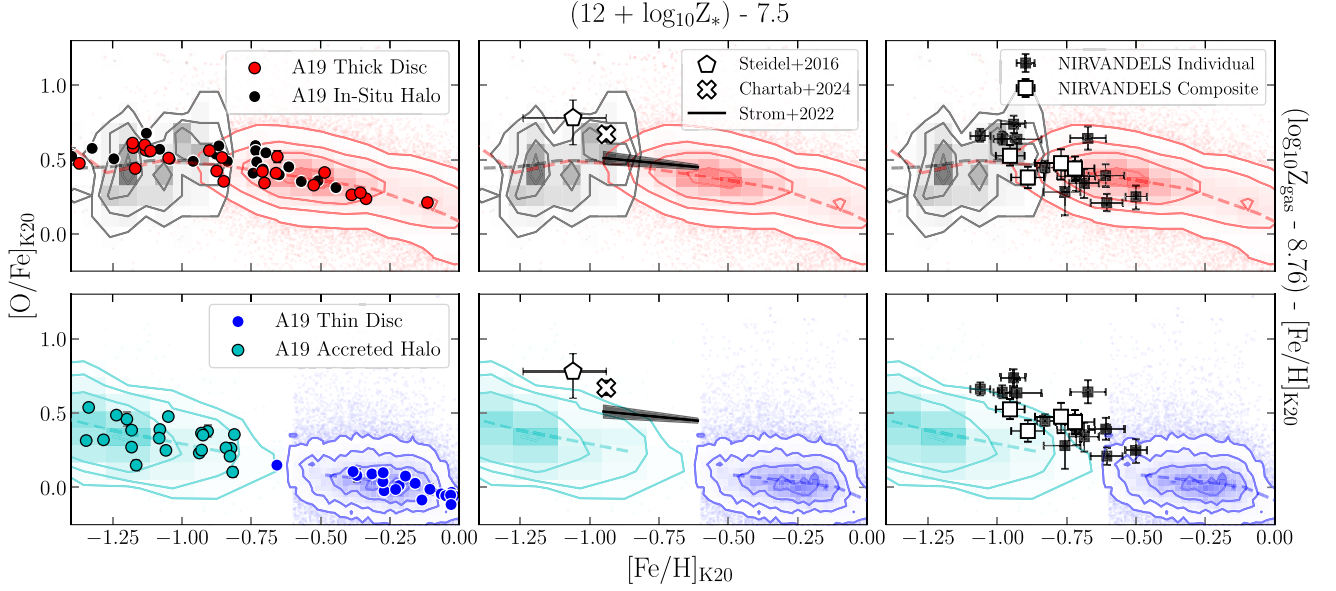


Figure 3. Density contours of the four MW structural components we consider in $[O/Fe]$ versus $[Fe/H]$ space using our cleaned GALAH catalogues after shifting into agreement with components in A19. *Left:* high resolution, 1D NLTE data for each component taken from the study of Amarsi et al. (2019) is over-plotted as the colour-coded points using their dynamical associations. The mean value of each component as a function of metallicity in GALAH DR3 is marked using a dashed line. Both GALAH and Amarsi et al. (2019) have been put on to the solar scale adopted by Kobayashi et al. (2020b) ('K20'). *Middle:* stacked data from the KBSS (Steidel et al. 2014) and LATIS surveys (Chartab et al. 2024) and the KBSS (oxygen, iron) mass-metallicity relation from (Strom et al. 2022) at $z \sim 2$ (shown in black, with the uncertainty in the relation shown as the shaded region). *Right:* the NIRVANDELS data ($z \sim 3$) from Stanton et al. (2024) for individual galaxies and composite data (stacked) is included as white squares, shifted to the K20 scale. All intermediate redshift data points have been corrected for dust depletion. **Note the excellent agreement between the GALAH DR3 abundances across metallicities and the A19 data points in each component after applying a global shift in $[O/Fe]_{K20}$ and the apparent overlap between the intermediate redshift data points and the high- α populations in the MW.**

Table 2. Summary of the cosmic noon galaxy abundances as absolute abundances ($A(X) = 12 + \log_{10}(X/H)$) and placed on the Kobayashi et al. (2020b) solar scale, where $A(Fe)_{\odot} = 7.50$ and $A(O)_{\odot} = 8.76$. Note that the dust depletion correction has been applied to the oxygen abundances listed in columns six and eight. The uncertainty on the correction (0.03 dex) has been included in the quoted uncertainties in these columns, adding the uncertainty in quadrature with the nominal abundance uncertainty. The same uncertainties listed in columns five and six can be applied to the corresponding solar-scaled abundances. To include more points from KBSS (Strom et al. 2022), the following equation yields $[O/Fe]_{K20}$ abundances for $[Fe/H]_{K20}$ values in the range of $[-0.95, -0.61]$, $[O/Fe]_{K20} = (0.48 \pm 0.03) - (0.18 \pm 0.08) \times ([Fe/H]_{K20} + 0.78)$.

Survey	Galaxy	z	Type	$A(Fe)$	$A(O)$	$[Fe/H]_{K20}$	$[O/Fe]_{K20}$
KBSS	LM1	2.40	Stack	$6.44^{+0.12}_{-0.18}$	$8.48^{+0.10}_{-0.10}$	-1.06	0.78
LATIS	—	2.50	Stack	$6.56^{+0.01}_{-0.01}$	$8.49^{+0.06}_{-0.06}$	-0.94	0.67
NIRVANDELS	KVS_055	3.09	Individual	$6.83^{+0.06}_{-0.06}$	$8.73^{+0.06}_{-0.07}$	-0.67	0.64
NIRVANDELS	KVS_085	3.19	Individual	$6.57^{+0.09}_{-0.07}$	$8.47^{+0.08}_{-0.09}$	-0.93	0.64
NIRVANDELS	KVS_204	3.47	Individual	$6.89^{+0.06}_{-0.06}$	$8.37^{+0.09}_{-0.10}$	-0.61	0.21
NIRVANDELS	KVS_208	3.19	Individual	$6.52^{+0.03}_{-0.03}$	$8.42^{+0.07}_{-0.08}$	-0.98	0.64
NIRVANDELS	KVS_227	3.61	Individual	$6.44^{+0.04}_{-0.04}$	$8.36^{+0.08}_{-0.08}$	-1.06	0.66
NIRVANDELS	KVS_248	3.08	Individual	$6.89^{+0.07}_{-0.06}$	$8.54^{+0.07}_{-0.07}$	-0.61	0.39
NIRVANDELS	KVS_312	3.24	Individual	$6.67^{+0.04}_{-0.03}$	$8.38^{+0.08}_{-0.09}$	-0.83	0.45
NIRVANDELS	KVS_391	3.07	Individual	$6.56^{+0.04}_{-0.05}$	$8.46^{+0.07}_{-0.07}$	-0.94	0.74
NIRVANDELS	34777	3.40	Individual	$6.74^{+0.05}_{-0.05}$	$8.29^{+0.24}_{-0.24}$	-0.76	0.28
NIRVANDELS	35212	3.40	Individual	$7.00^{+0.07}_{-0.09}$	$8.51^{+0.17}_{-0.18}$	-0.50	0.25
NIRVANDELS	33644	3.20	Individual	$6.81^{+0.06}_{-0.08}$	$8.42^{+0.18}_{-0.19}$	-0.69	0.35
NIRVANDELS	46857	3.35	Individual	$6.78^{+0.04}_{-0.04}$	$8.43^{+0.18}_{-0.17}$	-0.72	0.39
NIRVANDELS	k1	3.50	Stack	$6.55^{+0.05}_{-0.05}$	$8.33^{+0.06}_{-0.07}$	-0.95	0.53
NIRVANDELS	k2	3.50	Stack	$6.73^{+0.07}_{-0.07}$	$8.47^{+0.05}_{-0.05}$	-0.77	0.48
NIRVANDELS	m1	3.50	Stack	$6.61^{+0.06}_{-0.06}$	$8.25^{+0.07}_{-0.07}$	-0.89	0.38
NIRVANDELS	m2	3.50	Stack	$6.78^{+0.07}_{-0.07}$	$8.48^{+0.07}_{-0.07}$	-0.72	0.44

level of O enrichment for both the massive stars and the gas. This is the convention that we follow. We also focus primarily on samples where O and Fe were measured for the same galaxies. A summary table of abundances for the Cosmic Noon sample described in this section can be found in Table 2.

4.1 NIRVANDELS

Our principal comparison sample of distant galaxies comes from Cullen et al. (2021) and Stanton et al. (2024), who determined O and Fe abundances for a combined sample of 65 SFGs at $3.0 < z < 3.8$ (corresponding to lookback times of 11.3–11.9 Gyr). These galaxies were initially selected from the VANDELS survey⁵ (McLure et al. 2018; Pentericci et al. 2018; Garilli et al. 2021), an ultra-deep optical spectroscopic survey of the CANDELS CDFS and UDS fields undertaken using the VIMOS spectrograph (Le Fèvre et al. 2003; $R \sim 2500$) on ESO’s Very Large Telescope (VLT). The primary VANDELS targets were typical ‘main-sequence’ (i.e. typical SFR for a given M_*) SFGs for which ultra-deep (20–80 h) rest-frame UV were obtained. Rest-optical follow-up for a subset (dubbed NIRVANDELS) was later obtained with the Keck/MOSFIRE (McLean et al. 2012; $R \sim 3500$) and VLT/KMOS (Sharples et al. 2013; $R \sim 1985$) spectrographs, allowing key, abundance-sensitive H II region features to be observed. Detailed explanations of the sample selection, observations, and data reduction can be found in Cullen et al. (2021) and Stanton et al. (2024).

The Fe abundances were determined via full spectral fitting to the rest-frame FUV spectra using stellar population spectra generated using the high-resolution WM-Basic Starburst99 (S99) models without stellar rotation (Leitherer et al. 2010, 2014), assuming a constant SFH over 100 Myr; these models assume $Z_{\odot} = 0.014$ and $A(\text{Fe})_{\odot} = 7.50$. The forward-modelling approach adopted by NIRVANDELS included a flexible UV dust attenuation prescription, and the posterior distribution was sampled using nested-sampling software DYNESTY (Speagle 2020); full details of the spectral fitting approach are given in Cullen et al. 2019.

The O abundances were estimated from the [O II] $\lambda 3727$, [Ne III] $\lambda 3869$, H β and [O III] $\lambda 5007$ rest-frame optical emission lines using the Bian, Kewley & Dopita (2018) strong-line calibrations, which are T_e -based diagnostics calibrated using $z \sim 0$ galaxies that occupy the same region as $z \sim 2$ –3 galaxies in the so-called ‘BPT diagram’ [which compares $\log_{10}([\text{N II}]/\text{H}\alpha)$ and $\log_{10}([\text{O III}]/\text{H}\beta)$; Baldwin, Phillips & Terlevich 1981; Veilleux & Osterbrock 1987]. Some of the individual NIRVANDELS galaxies have line ratios outside the range calibrated by Bian et al. (2018) and require extrapolation, which may introduce some uncertainty.

Of the full sample, 12/65 galaxies yielded measurements of both O and Fe abundances, with 38/65 individual determinations of O and 17/65 individual determinations of Fe. To leverage the full sample, four composite spectra were created via stacking, from which robust O and Fe abundances were measured. In our present analysis, we make use of the 12 individual galaxies with both O and Fe abundance measurements, as well as measurements from the four composite spectra. The basic demographic properties of the individual NIRVANDELS galaxies and composite spectra used in the present study are shown in Fig. 4, where both sSFR and M_* are reported assuming a Chabrier (2003) stellar initial mass function (IMF). Many of these galaxies have high sSFRs ($\gtrsim -8.5$), consistent with short gas depletion time-scales and young ages.

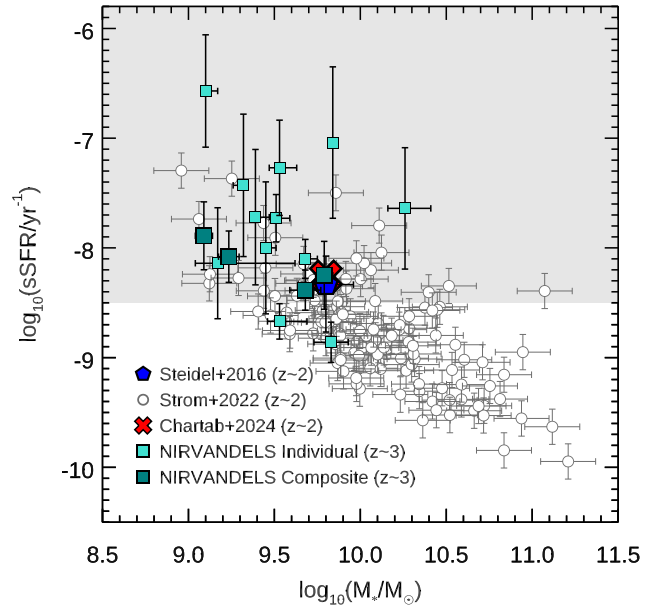


Figure 4. The specific star formation rates ($\text{sSFR} \equiv \text{SFR}/M_*$) and stellar masses (M_*) for the Cosmic Noon samples at $z \sim 2$ (at a lookback time of ~ 10.8 Gyr) and $z \sim 3$ (at a lookback time of ~ 11.3 Gyr). Measurements from composite spectra reported by Steidel et al. (2016) and Chartab et al. (2024) are shown as the blue pentagon and red cross, respectively; the full KBSS galaxy sample from Strom et al. (2022) is shown as the open circles. Individual galaxies and composite spectra from NIRVANDELS (Cullen et al. 2021; Stanton et al. 2024) are shown as the small light teal squares and large dark teal squares, respectively. Many of these galaxies have $\text{sSFR} \gtrsim -8.5$ (highlighted by the grey shaded band), which imply formation time-scales less than expected minimum Type Ia SNe delay times. It follows that the chemistry of these galaxies would be dominated by CCSNe enrichment (Chruslińska et al. 2024).

To accurately compare the NIRVANDELS galaxies with the local samples introduced in the previous section, we must place the reported abundances on the K20 scale. Fortunately, the electron temperature (T_e), or ‘direct,’ method of determining O abundances does not assume an intrinsic solar scale but instead uses measurements of the oxygen lines (of various ions) relative to hydrogen recombination lines and the emissivities calculated using T_e and n_e to directly determine O/H. As a result, strong-line diagnostics based on T_e samples already produce absolute $A(\text{O})$ values, so that $[\text{O}/\text{H}]_{\text{K20}} = A(\text{O}) - A(\text{O})_{\odot, \text{K20}}$.

To calculate the absolute Fe abundances from the model comparisons, we use the following equation:

$$A(\text{Fe}) = \log_{10}(Z_*/Z_{\odot, \text{S99}}) + A(\text{Fe})_{\odot, \text{S99}}. \quad (1)$$

To get $[\text{Fe}/\text{H}]_{\text{K20}}$, we then subtract $A(\text{Fe})_{\odot, \text{K20}}$. In this case, because $A(\text{Fe})_{\odot, \text{S99}} = A(\text{Fe})_{\odot, \text{K20}}$, we can simply adopt $[\text{Fe}/\text{H}]_{\text{K20}} = \log_{10}(Z_*/0.014)$.

4.2 Keck Baryonic Structure Survey

Steidel et al. (2016) inferred O and Fe abundances using composite rest-UV and rest-optical spectra of a sample of 30 SFGs at $\langle z \rangle = 2.40 \pm 0.11$ (e.g. a lookback time of 10.8 Gyr) that were observed as part of the Keck Baryonic Structure Survey (KBSS; Rudie et al. 2012; Steidel et al. 2014). KBSS comprises 15 fields containing luminous quasars at $z \gtrsim 2.7$ and rest-UV colour-selected galaxies at $1.5 \lesssim z \lesssim 3.5$ that were targeted for spectroscopic follow-up using Keck/LRIS

⁵<https://doi.org/10.18727/archive/53>

(Oke et al. 1995; Steidel et al. 2004; $R \sim 1500$) and Keck/MOSFIRE. The galaxies that were used to construct the composite spectrum are representative of the parent sample, reflected in the location of the Steidel et al. (2016) point (blue pentagon) relative to a larger sample of KBSS galaxies (open circles) in Fig. 4. Detailed descriptions of the sample selection, observations, and spectroscopic data reduction can be found elsewhere (e.g. Steidel et al. 2010, 2014; Strom et al. 2017), but we review the abundance measurements here.

As for NIRVANDELS, the Fe abundance for the Steidel et al. (2016) stack was determined by comparing the FUV composite spectrum with dust-reddened model spectra from both S99 and BPASS (Binary Population and Spectral Synthesis, v2.0; Eldridge & Stanway 2016; Stanway, Eldridge & Becker 2016). Notably, BPASS assumes different solar values from S99, using $Z_{\odot} = 0.02$ and $A(\text{Fe})_{\odot} = 7.56$. The comparison between the Steidel et al. (2016) stack and the SPS models spanned a range in stellar metallicity Z_* , IMF slopes, and upper-mass cut-offs for the IMF. Using a χ^2 -minimization technique, Steidel et al. (2016) found that the observed stellar photospheric absorption and wind lines were best matched by models with stellar metallicities in the range $Z_* = 0.001\text{--}0.002$ for both S99 and BPASS. The authors ultimately adopt the BPASSv2.0 models with an upper-mass cut-off of $300 M_{\odot}$ and an IMF index of -2.35 . Using the same translation described above, $[\text{Fe}/\text{H}] = \log_{10}(0.0015/0.02) + 7.56 - 7.5 = -1.06^{+0.12}_{-0.18}$.

The O abundance is determined using the bright emission lines in the rest-optical spectrum by comparing the measured line fluxes (relative to $\text{H}\beta$) with predictions from CLOUDY (v13.02; Ferland et al. 2013) photoionization models. The CLOUDY models use the best-fitting model stellar spectrum from BPASS as the input ionizing radiation field and allow the gas-phase metallicity (Z_{neb}) and the ionization parameter ($U \equiv n_{\gamma}/n_{\text{H}}$) to vary. These models assumed a plane-parallel geometry and $n_{\text{H}} = 300 \text{ cm}^{-3}$, to be consistent with the electron densities⁶ measured for KBSS galaxies (Strom et al. 2017). The authors find that the photoionization model predictions for $Z_{\text{neb}}/Z_{\odot} \approx 0.5$ and $\log U = -2.8$ are in good agreement with the location of the composite spectrum in multiple line-ratio diagrams. Because CLOUDY assumes $A(\text{O})_{\odot} = 8.69$, this results in a ‘best-fitting’ gas-phase $A(\text{O}) = 8.38 \pm 0.10$.

We also use chemical abundance measurements for a sample of individual SFGs from KBSS (Strom et al. 2022), which are shown in Fig. 4 as open circles. This study used a custom photoionization model method introduced by Strom et al. (2018) to simultaneously infer O, N, and Fe abundances, as well as ionization parameter U , for ~ 200 individual galaxies. In this method, the full suite of rest-optical emission lines is compared with predicted nebular spectra from CLOUDY to determine the most likely combination of Z_{neb} , Z_* , U , and $\log(\text{N}/\text{O})$; the input SPS models are taken from BPASS, the same as for Steidel et al. (2016). Z_{neb} and Z_* are converted to O/H and Fe/H as already described. Strom et al. (2022) use these measurements to investigate multiple elemental abundance scaling relations with respect to M_* (i.e. the mass–metallicity relation, or MZR), finding that the O-MZR and Fe-MZR have similar slopes, but that the Fe-MZR is offset toward lower abundances relative to solar. In other words, KBSS galaxies have significantly less Fe than O at all M_* , compared to the Sun.

The two MZRs are expressed as $[\text{O}/\text{H}] = \alpha_{\text{O}} + \beta_{\text{O}}x$ and $[\text{Fe}/\text{H}] = \alpha_{\text{Fe}} + \beta_{\text{Fe}}x$, where $x = \log(M_*/M_{\odot}) - 10$. Using these equations, we can construct a ‘locus’ in the Tinsley–Wallerstein diagram with

the following form:

$$[\text{O}/\text{Fe}] = (\alpha_{\text{O}} - \alpha_{\text{Fe}}) + \left(\frac{\beta_{\text{O}}}{\beta_{\text{Fe}}} - 1 \right) ([\text{Fe}/\text{H}] - \alpha_{\text{Fe}}). \quad (2)$$

After accounting for the difference between the $Z_{\odot} = 0.014$ adopted by Strom et al. (2022) and $Z_{\odot, \text{BPASS}} = 0.02$, and shifting on to the K20 scale, the KBSS MZRs have the following parameters:

$$\begin{aligned} \alpha_{\text{O}} &= -0.41 \pm 0.02 \\ \beta_{\text{O}} &= 0.14 \pm 0.05 \\ \alpha_{\text{Fe}} &= -0.78 \pm 0.02 \\ \beta_{\text{Fe}} &= 0.17 \pm 0.05, \end{aligned} \quad (3)$$

so that $[\text{O}/\text{Fe}] = (0.37 \pm 0.03) - (0.18 \pm 0.08) ([\text{Fe}/\text{H}] + 0.78)$.

4.3 Ly α tomography IMACS survey

Chartab et al. (2024) also measure $A(\text{Fe})$ for Cosmic Noon galaxies, applying the method first introduced by Steidel et al. (2016) and later employed by NIRVANDELS to a sample of ~ 3000 SFGs at $z \sim 2.5$ (corresponding to a lookback time of ~ 10.9 Gyr) observed as part of the Ly α Tomography IMACS Survey (LATIS). As the survey name implies, the rest-UV spectra of the galaxies were observed with Magellan/IMACS (Dressler et al. 2011; $R \sim 1000$). Chartab et al. (2024) create a composite spectrum of the entire sample (with the average sSFR and M_* shown as the red cross in Fig. 4) and use BPASS models to determine the stellar metallicity. They find an average $[\text{Fe}/\text{H}] = -0.94 \pm 0.01$, after accounting for the difference between the $Z_{\odot} = 0.0142$ they assume and $Z_{\odot, \text{BPASS}}$ and shifting on to the K20 scale. Based on a composite rest-optical spectrum of 17 LATIS galaxies that were previously observed with Keck/MOSFIRE (Kriek et al. 2015), they find $A(\text{O}) = 8.39 \pm 0.05$, using the N2 calibration from Bian et al. (2018).

4.4 Towards a common abundance scale & systematic uncertainties II: high-redshift sample

The resolved stellar abundances used in this study (Section 3) all rely on the same fundamental technique, namely equivalent width measurements of stellar absorption features associated with specific atomic transitions. In contrast, the O and Fe abundances of SFGs, including our Cosmic Noon samples, are determined using a variety of techniques and rely on both measurements of the ionized gas in H II regions and the stars illuminating that gas. Differences in the methods used to derive their $A(\text{O})$ and $A(\text{Fe})$ can lead to significant – although not always well quantified – systematic uncertainties (see, e.g. Maiolino & Mannucci 2019; Chruślińska et al. 2024).

Regardless of the method, we must account for metal depletion on to dust grains when determining total gas-phase abundances. In practice, this is often neglected in extragalactic studies, but given our explicit goal of comparing representative abundance patterns in distant and nearby systems, using methods that probe *different* phases, we cannot ignore the metals locked in dust. This is especially important for $A(\text{O})$, as ~ 20 per cent of oxygen can be contained in dust grains, with the exact amount depending weakly on the total amount of oxygen in the gas (e.g. Peimbert & Peimbert 2010; Peña-Guerrero et al. 2012). We account for this effect by adopting the scheme from Peimbert & Peimbert (2010), where the depletion of O in dust grains is 0.10 ± 0.03 in ‘intermediate O/H’ environments ($7.8 < 12 + \log \text{O}/\text{H} < 8.3$) and 0.11 ± 0.03 in ‘high O/H’ environments ($12 + \log \text{O}/\text{H} > 8.3$). The result of this correction is to *increase* all $[\text{O}/\text{H}]$ and $[\text{O}/\text{Fe}]$ values by ~ 0.1 dex. In contrast to $A(\text{O})$,

⁶For ionized gas, $n_{\text{H}} \approx n_{\text{e}}$.

A(Fe) is unaffected by dust depletion because it is measured directly from the stellar photospheres and is, therefore, already comparable to A(Fe) measured for the resolved stellar populations. The K20-scaled abundance measurements for our Cosmic Noon sample, now corrected for O depletion on to dust, are shown in the centre and right panels of Fig. 3.

Aside from depletion on to dust, there are additional factors that may bias abundance determinations in distant galaxies. For example, the choice of SPS model and, e.g. assumptions about binary evolution, stellar rotation and winds, and the IMF can influence the measured A(Fe). In cases where multiple models can be directly compared to the non-ionizing UV spectrum (e.g. Steidel et al. 2016; Cullen et al. 2019), Z_* appears to be moderately sensitive to differences in the models, with systematic offsets of ~ 0.1 – 0.2 dex (compare Fe-MZR in the left and right columns in Fig. 7). Methods relying on the shape of the ionizing radiation as a proxy for Z_* (e.g. Strom et al. 2018, 2022; Sanders et al. 2020) show larger differences, as predictions for the ionizing UV spectrum vary more widely from model to model. Furthermore, Strom et al. (2018) found that the [Fe/H] inferred using their photoionization model method tended to be higher than the [Fe/H] determined from a non-ionizing UV composite spectrum of similar galaxies (Steidel et al. 2016). For example, both Strom et al. (2018) and Steidel et al. (2016) analyse $z \sim 2$ galaxies from KBSS and find $[O/H] \simeq -0.38$ at $\log_{10}(M_*/M_\odot) = 9.8$ (the average M_* for the composite spectrum). However, these samples are considerably offset in the centre panels of Fig. 3. This is because Steidel et al. (2016) report a [Fe/H] that is ~ 0.3 lower than the Fe-MZR from Strom et al. (2018) at the same M_* ; the effect is to move the Strom et al. (2018) locus to lower [O/Fe] and higher [Fe/H] (down and to the right). Interestingly, this difference is greatly reduced when the photoionization model method is used to analyse the higher S/N composite spectrum itself, perhaps indicating a need for higher quality observations when using this more indirect method to determine A(Fe).

A separate source of uncertainty in A(O) measurements is the choice of strong-line calibration (e.g. Kewley & Ellison 2008; Kewley, Nicholls & Sutherland 2019; Maiolino & Mannucci 2019). These are used in most studies of faint and/or distant galaxies, because neither metal recombination lines nor the T_e -sensitive auroral lines are bright enough to be routinely detected in individual objects. Strong-line diagnostics may be calibrated using T_e -based abundances or photoionization models, but those based on auroral lines typically lead to lower A(O) than model-based methods for the same objects. Unfortunately, it is difficult to ascertain ‘ground truth,’ because there is also a discrepancy between T_e -based abundances (and the strong-line diagnostics based on them) and those inferred from oxygen recombination lines. Both photoionization model and recombination line-based measurements are often significantly higher (by ≈ 0.20 – 0.24 dex) than methods anchored using T_e . This offset is thought to arise due to temperature fluctuations in the ionized gas (e.g. Peimbert 1967; Croxall et al. 2013; Méndez-Delgado et al. 2023): because less enriched gas is hotter and can more efficiently populate the upper energy levels in metal ions, it will produce more auroral line emission, tending to bias A(O) low. The difference between T_e -based abundances and recombination line abundances is a longstanding challenge in studies of nearby nebulae, referred to as the Abundance Discrepancy Factor, or ADF (see Tsamis et al. 2003; García-Rojas & Esteban 2007). However, the exact value of the ADF is subject to vigorous debate and likely differs from H II region to H II region, depending on the local ISM conditions (e.g. Mesa-Delgado, Esteban & García-Rojas 2008; Peña-Guerrero et al. 2012); indeed, the ADF is found to be negligible in some cases (e.g.

Toribio San Cipriano et al. 2017; Chen et al. 2023). Consequently, we opt not to incorporate any systematic shift to account for the ADF in our analysis and instead only apply the dust depletion correction introduced at the beginning of this section.

Finally, most studies of distant galaxies have used *locally* ($z \sim 0$) calibrated strong-line diagnostics, which can introduce unknown systematic biases when applied to $z \gtrsim 0$ galaxies with significantly different physical conditions. Bian et al. (2018) attempted to circumvent this issue by identifying local analogues in line-ratio space, although their calibrations differ significantly from those based on photoionization models of $z \sim 2$ galaxies (Strom et al. 2018). *JWST* promised to mitigate these concerns by enabling new *in situ* calibrations for strong-line diagnostics, based on T_e -based oxygen abundances from a representative sample of high- z galaxies, and multiple Cycle 1 proposals were approved to pursue this goal. Early attempts based on supersets of all auroral line measurements to date have already been published (e.g. Laseter et al. 2024; Sanders et al. 2024; Scholte et al. 2025), although they do not yet extend to the region of parameter space occupied by most L^* galaxies at $z \sim 2$ – 3 ; if we use these calibrations, the A(O) measurements for our Cosmic Noon sample appear shift upward by ~ 0.1 dex (compare the left and centre columns of Fig. 7). As the community converges on new, more appropriate high- z strong-line calibrations, it will be important to revisit previously studied samples, including those introduced here.

5 COMPARING ABUNDANCE PATTERNS

With our local and Cosmic Noon data sets reconciled and placed on the same scale, we are prepared to discuss similarities and differences across the two populations using the Tinsley–Wallerstein diagram. The chemical evolution of our MW components and Local Group galaxies is presented in Fig. 5. The title of each panel in Fig. 5 is the average total stellar mass (M_*) of the local galaxies included in that panel. We assume a total stellar mass of $M_{MW,*} = 5.43 \times 10^{10} M_\odot$ (McMillan 2017) for the MW, $M_{M31,*} = 12.5 \times 10^{10} M_\odot$ for M 31 (Tamm et al. 2012), $M_{LMC,*} = 2.7 \times 10^9 M_\odot$ for the LMC (Shipp et al. 2021) and $M_{SMC,*} = 3.1 \times 10^8 M_\odot$ for the SMC (Besla 2015). Given both the Sgr and GSE galaxies are either in the process of being disrupted, or are totally disrupted, we assume initial masses of $M_{Sgr,*} = 2 \times 10^8 M_\odot$ for Sgr (Vasiliev, Belokurov & Erkal 2021) and $M_{GSE,*} = 1.5 \times 10^8 M_\odot$ (Lane, Bovy & Mackereth 2023), respectively. The Cosmic Noon galaxy compilation is over-plotted in each panel of Fig. 5, with the $z \sim 2$ galaxies shown in the top row and the $z \sim 3$ galaxies below. All Cosmic Noon galaxies are shaded by their total stellar mass.

5.1 Cosmic Noon and present-day galaxies

For the Cosmic Noon sample, we see clear trends with mass across all three panels in Fig. 5, consistent with expectations from GCE models. In the $z \sim 2$ sample (top row), the intermediate mass Steidel et al. (2016) and Chartab et al. (2024) points show clear α -enhancement, consistent with being massive SFGs. The KBSS points from Strom et al. (2022), while systematically lower in [O/Fe]_{K20} for reasons discussed in Section 4.4, are also significantly α -enhanced, even as their overall metallicity increases with increasing mass – indicative of enhanced SF at comparatively high stellar masses (up to $\sim 10^{11} M_\odot$). Similarly, the $z \sim 3$ galaxies (bottom row), show a clear gradient of increasing mass with increasing metallicity, which was first noted in Stanton et al. (2024) and is again consistent with GCE models. Note that the position of the most massive and chemically evolved NIRVANDELS galaxy, KVS_055 (the darkest NIRVANDELS data

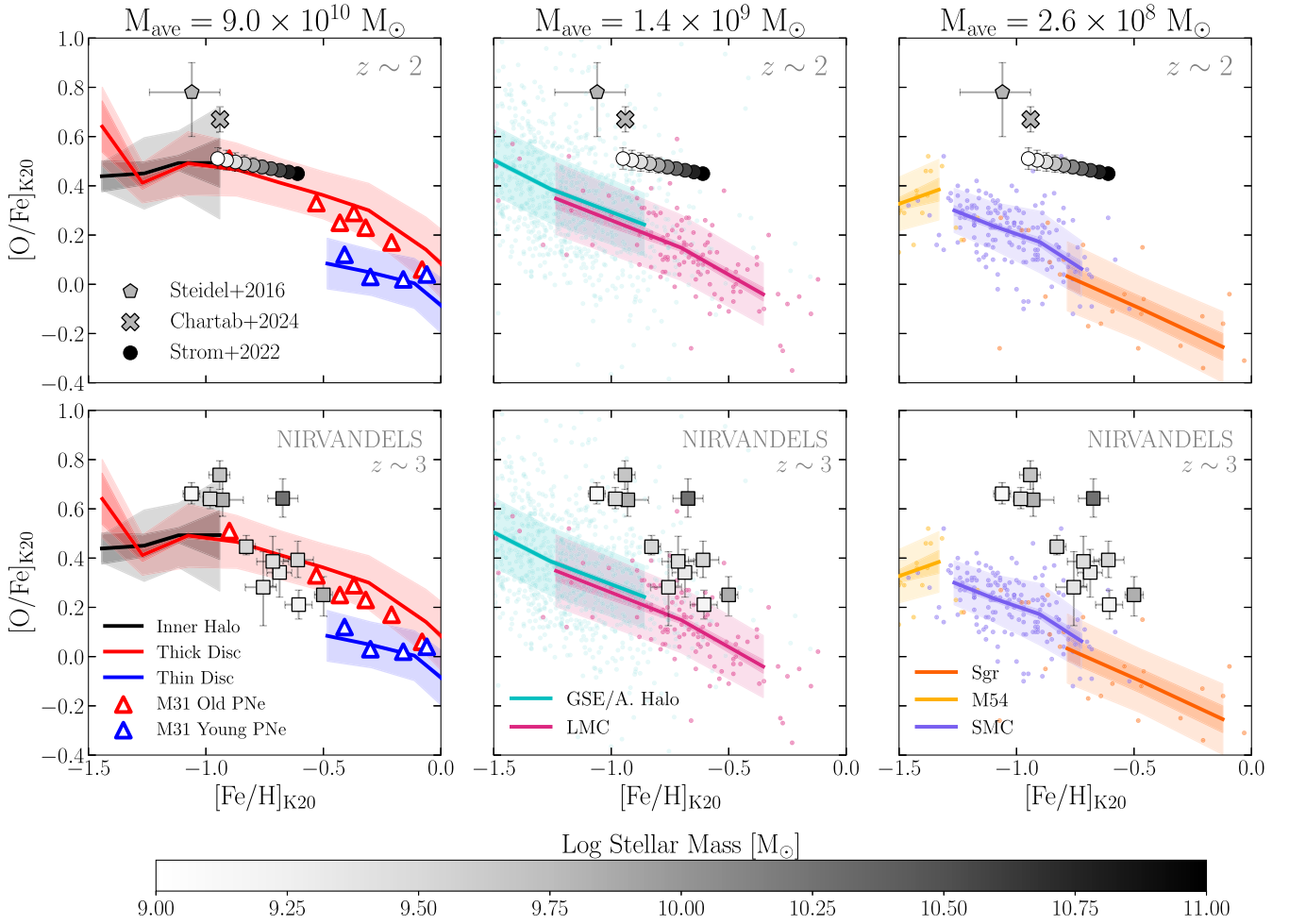


Figure 5. The chemical evolution of the MW and four local dwarf galaxies in $[\text{O}/\text{Fe}]_{\text{K20}}$ versus $[\text{Fe}/\text{H}]_{\text{K20}}$ is shown alongside the Cosmic Noon sample (coloured by mass) and data for the two PNe populations in M 31. The $z \sim 2$ Cosmic Noon sample is shown in the top row, while the $z \sim 3$ sample is shown in the bottom row. The Strom et al. (2022) points sample the (oxygen and iron) mass–metallicity relations derived in that study. The title for each panel is the average total M_* for the local galaxies shown in each (references are given in the text). *Left:* data for three MW components (from our GALAH sample) represented as the binned mean (bin sizes of 0.2–0.3 dex depending on the component) with the median absolute deviation shown as the shaded region. Medians of the young and old PNe nebulae populations in M 31 in the radial range of 3–14 kpc from the study of Bhattacharya et al. (2022) and mapped to $[\text{O}/\text{Fe}]$ and $[\text{Fe}/\text{H}]$ in Kobayashi et al. (2023) are marked with the blue and red triangles, respectively. *Middle:* the evolution of the accreted halo/GSE (from GALAH, cyan) and the LMC (Pompéia et al. 2008; Van der Swaelmen et al. 2013; pink) shown as the binned mean, standard deviation weighted by the number of stars per bin (dark shaded region) and standard deviation (light shaded region). The raw data points are plotted underneath as coloured points. *Right:* same as the central panel except the Sgr dGal (orange) is shown alongside its nuclear star cluster [M 54 (yellow); Carretta et al. 2010] and the SMC (Mucciarelli et al. 2023). **Note the excellent agreement between the M 31 high- and low- α PNe and the high- and low- α discs in the MW (first column), the appearance of similar $[\text{O}/\text{Fe}]_{\text{K20}}$ values at fixed metallicities between different galaxies despite distinct star formation histories (columns two and three) and the gradual depletion in $[\text{O}/\text{Fe}]_{\text{K20}}$ as a function of decreasing stellar mass (all three columns).**

point in Fig. 5, $M_* = 1.6 \times 10^{10} M_\odot$) is both at high $[\text{O}/\text{Fe}]_{\text{K20}}$ and high $[\text{Fe}/\text{H}]_{\text{K20}}$.

When we compare the $z \sim 2$ – 3 galaxies and different MW components (shown in the centre and right-most columns in Fig. 3 and the left-most column of Fig. 5), we see that they all show good agreement with the high- α disc and α -rich inner halo and have significantly higher $[\text{O}/\text{Fe}]_{\text{K20}}$ at fixed $[\text{Fe}/\text{H}]_{\text{K20}}$ than the lower mass galaxies shown in the centre and right panels of Fig. 5. Given the average NIRVANDELS galaxy mass is $M_{\text{ave},*} = 3.35^{+0.87}_{-0.39} \times 10^9 M_\odot$ at $z \sim 3$, a time when the MW was likely significantly smaller, we would expect these galaxies to show a higher level of α -enhancement relative to the MW *if* we assume that they have had a constant SFR. If the NIRVANDELS galaxies have experienced a SFH that includes an early strong SF episode, potentially followed

by additional bursts, their chemistry may include some contribution from an older population of stars which have been polluted by Type Ia SNe (analogous to the $z \sim 1.3$ – 4 galaxies in $[\text{O}/\text{Ar}]$ versus $[\text{Ar}/\text{H}]$; Bhattacharya et al. 2025; Stanton et al. 2025). We revisit the low- α NIRVANDELS galaxies in upcoming sections, exploring whether different abundance methodologies affect their location in $[\text{O}/\text{Fe}]_{\text{K20}}$ versus $[\text{Fe}/\text{H}]_{\text{K20}}$.

5.2 The Milky Way and M 31

Comparing the MW to M 31 directly, the left-most panel of Fig. 5 reveals excellent agreement between the MW high- and low- α discs and the M 31 old (>4.5 Gyr) and young (<2.5 Gyr) PNe, respectively. We interpret this as further support for the existence of

high- α and low- α chemical sequences in the inner regions of the disc of M 31 (Kobayashi et al. 2023). Note that although both chemical sequences in M 31 are dynamically hot, beyond a galactocentric radius of 14 kpc the older population of PNe display a higher total velocity dispersion than the younger PNe – suggesting that, as in the MW, the high- α PNe belong to a thick disc population as first noted by Merrett et al. (2006) and later confirmed by Dorman et al. (2015) and Bhattacharya et al. (2019b.) Interestingly, the age ranges provided by the M 31 PNe date both components as being significantly younger than the MW high- α and low- α disc. In the MW, high- α disc ages peak sharply around ~ 11 Gyr, while the low- α disc displays a broad range of ages, peaking roughly around ~ 5 Gyr for stars with $[\alpha/\text{Fe}] < 0.2$ using astroseismic ages from Miglio et al. (2021).

While the range of ages is quite small for the PNe associated with the low- α disc of M 31, the range for our own MW low- α disc is substantially broader, signifying extended star formation over ~ 10 Gyr. This opposition is reflected in the high- α PNe population as well, where the broad allowable age range is much larger than the MW high- α disc where Miglio et al. (2021) predict SF took place over a period of *only* 1.5 Gyr. Finally, Miglio et al. (2021) predict a gap in SF between the two MW discs, which also appears to be the case in M 31 given the two PNe age ranges.

The origin of the high and low- α sequences in both the MW and M 31 is still the subject of debate. Despite this, the results shown in Fig. 5, suggest the same outcome (at least chemically) on different time-scales. In the case of M 31, results from both cosmological simulations and observations of M 31 GC populations, PNe and RGB stars, suggest a recent, and massive, merger took place ~ 2 Gyr ago (D’Souza & Bell 2018; Hammer et al. 2018; Mackey et al. 2019; Dey et al. 2023; Tsakonas et al. 2025). This is roughly concurrent with the age of the low- α PNe, and consistent with PNe kinematics (Bhattacharya et al. 2023), driving the two infall GCE model first presented in Arnaboldi et al. (2022) and further investigated in Kobayashi et al. (2023). In the MW, the last major merger with the GSE progenitor likely took place after the appearance of the high- α , thick disc (explaining the appearance of the ‘Splash’ stars, with thick-disc chemistry and heated kinematics; Belokurov et al. 2020). Given the range of ages for low- α disc stars in Miglio et al. (2021, see their fig. 13), some low- α disc stars may have already formed at the time of the merger. While low- and high- α sequences appear in both the MW and M 31 (and in other galaxies, e.g. UGC 10738, ESO 544-27, and IC 1553, where, in every case, dynamically hot high- α populations are found alongside dynamically colder, low- α populations; Scott et al. 2021; Somawanshi et al. 2024, 2025), it is unlikely that the physical cause of the two sequences and any relation to their scale heights is universal.

5.3 Local Group dwarf galaxies and the GSE

Moving to the second and third panels in Fig. 5, we explore similarities between our Local Group dGals. The second panel presents the chemical evolution of our accreted halo sample from GALAH in cyan, with the bulk of the contribution in this metallicity range assumed to be associated with the GSE dGal (e.g. Feuillet et al. 2020; Monty et al. 2020; Buder et al. 2022; Myeong et al. 2022). The LMC is also shown in this plot, combining both the disc and bar populations from Pompéia et al. (2008) and Van der Swaelmen et al. (2013). Note that the population is dominated primarily by the bar population (99/116 stars), which likely represents the most recent episode of star formation in the LMC (Van der Swaelmen et al. 2013). To interpret the similarities and differences between the

galaxies in this space, we benefit from the resolved star formation histories of the two systems.

Beginning with the LMC, both the LMC and SMC have been called ‘lazy giants’ due to their relatively delayed SFHs. In the LMC, SF likely peaked only ~ 2 Gyr ago (Nidever et al. 2020; Hasselquist et al. 2021). Note however that we only see a weak rise in $[\text{O}/\text{Fe}]_{\text{K}20}$ at high metallicities (related to a burst of SF) seen in the APOGEE data and used to derive the delayed SFH in Hasselquist et al. (2021). As a result of the slow SF, the appearance of the low- α knee in the LMC occurs at very low metallicities, $[\text{Fe}/\text{H}]_{\text{K}20} < -2$ (Nidever et al. 2020), after which the LMC $[\text{O}/\text{Fe}]_{\text{K}20}$ values continue to decrease.

The SFH history of GSE likely truncated sometime between 8–10 Gyr ago ($z \sim 2$), concurrent with its infall on to the MW (Fattahi et al. 2019; Montalbán et al. 2021; Naidu et al. 2021). However, studies have suggested chemical evidence for a recent starburst in the MW (the component referred to as ‘Eos’; Myeong et al. 2022; Chen, Ting & Hayden 2024; Ciucă et al. 2024; Davies et al. 2025; Matsuno et al. 2024), possibly triggered by the infall of GSE. The presence of young stars on GSE-like orbits may support a scenario where star formation was triggered in both the MW and GSE and was more extended than once thought (Horta et al. 2024). Regardless of the true SFH of the GSE, be it early truncated SF, or early formation with a secondary burst triggered by infall on to the MW, it was undeniably more efficient at forming stars at *early* times than the LMC. This is supported by the location of the low- α knee in GSE stars occurring at $[\text{Fe}/\text{H}] \sim -1.5$ (Myeong et al. 2019; Monty et al. 2020), 0.5 dex higher than the LMC.

Finally, in the third panel we show the sequences of Sgr (and its nuclear star cluster, M 54) and the SMC. The SMC also likely had an unusual SFH (Nidever et al. 2020; Hasselquist et al. 2021), with a late stage burst similar to the LMC (and likely related to an interaction between the two). As in the case of GSE, Sgr has a SFH greatly influenced by its interaction with the MW. SFHs derived both photometrically and through chemical evolution modelling agree that the majority of SF in Sgr ceased ~ 5 Gyr ago, likely related to infall on to the MW (de Boer, Belokurov & Koposov 2015; Hasselquist et al. 2021). The appearance of secondary star formation episodes (possibly related to continued interaction with the MW) is uncertain.

In summary, the diversity of SFHs in the Local Group – driving distinct chemical evolution in $[\text{O}/\text{Fe}]_{\text{K}20}$ versus $[\text{Fe}/\text{H}]_{\text{K}20}$, as shown in Fig. 5 and highly affected by their dynamical histories, supports the assertion that galaxies at Cosmic Noon and beyond likely also experienced more complex SFHs beyond simple assumptions of constant SFRs. This point will become increasingly important as *JWST* observes progressively less massive galaxies at increasing redshifts and we seek to interpret their SFHs.

6 CHRONO-CHEMICAL ABUNDANCE TRENDS

We now attempt to place our Local and Cosmic Noon samples into the same chrono-chemical context using ages for MW field stars and GCs. We focus solely on the NIRVANDELS $z \geq 3$ galaxies, based on the assumption that the MW was relatively simple at that time, composed only of the inner halo and early high- α disc, and had not yet merged with GSE. In contrast, based on estimates of the last major merger (10–12 Gyr ago; Fattahi et al. 2019), it is likely that the MW evolved significantly at $z \sim 2$, so we opt to neglect the $z \sim 2$ galaxies in this section.

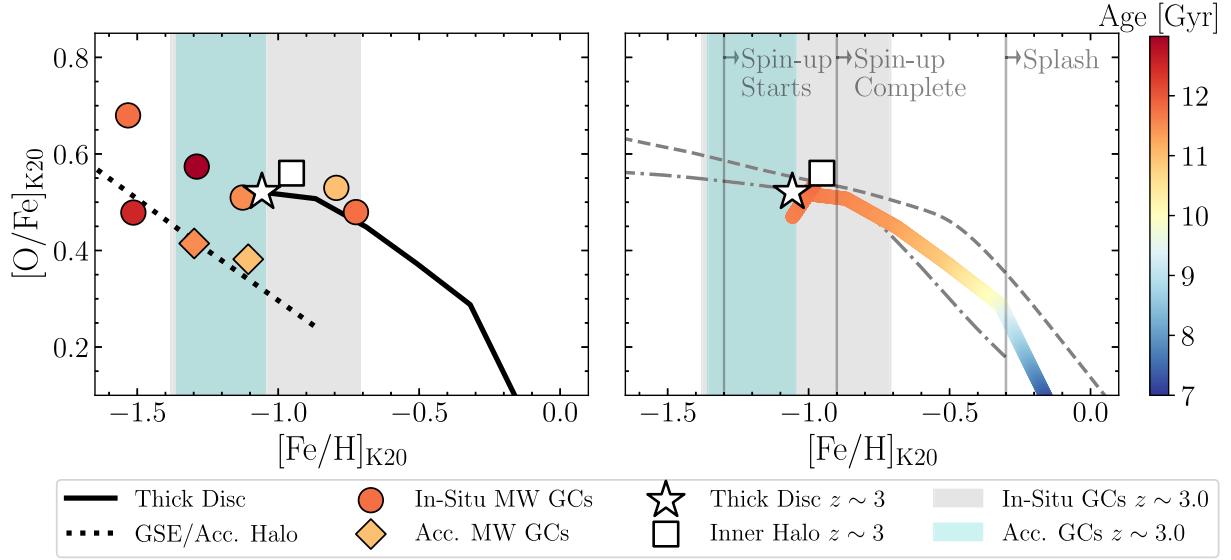


Figure 6. The chrono-chemical evolution of MW inner halo and high- α disc stars (black line in the left panel, rainbow line in the right panel), where the mean age is calculated for 0.2 dex bins in metallicity for both samples to determine the age gradient in the left panel. The location of both samples at $z \sim 3$ using the Hayden et al. (2022) ages are marked with a square and star, respectively. Ages from VandenBerg et al. (2013) are shown for the *in situ* GC population (circles), with the location of the clusters shifted by +0.1 dex in $[\text{O}/\text{Fe}]_{\text{K}20}$, as discussed in Section 3. The grey shaded region marks the range in $[\text{Fe}/\text{H}]$ associated with GC ages in the range of 11.5–12 Gyr (close to $z \sim 3$). GCs associated with the GSE merger by Massari et al. (2019) and Myeong et al. (2019) are marked with diamonds. The cyan shaded region marks the range in $[\text{Fe}/\text{H}]$ associated with GSE GC ages in the range of 11–11.5 Gyr (the only available ages). GCE models from K20 for the MW thick disc (dot-dashed line) and bulge (dashed line) are also included. The mean evolution of the GSE sample in GALAH is shown with the dotted line. The estimated location of the beginning and end of the emergence of the high- α disc, or ‘spin-up’ from Belokurov & Kravtsov (2022) in metallicity are marked in the left column as vertical lines. The location of the completion of the ‘Splash’ heating of the high- α disc in metallicity is also marked via a vertical line to give context to the MW’s evolution. **Note the agreement between the location for the MW at $z \sim 3$ in $[\text{O}/\text{Fe}]_{\text{K}20}$ and $[\text{Fe}/\text{H}]_{\text{K}20}$ predicted by the field stars (square and star) and the population of *in situ* GCs (black shaded region) and that these predictions place the MW just prior to the completion of the formation of the high- α (thick) disc at $z \sim 3$.**

6.1 Look back times and isochronal ages

To convert the NIRVANDELS spectroscopic redshifts to look back times, we use the ASTROPY FlatLambdaCDM (Astropy Collaboration 2022) cosmological model which assumes a flat cosmology, a Hubble constant of $70 \text{ km s}^{-1} \text{ Mpc}^{-1}$ and a matter density $\Omega_m = 0.3$ at $z = 0$. We assume a total age for the Universe of 13.6 Gyr. Ages for MW stars are taken from the study of Hayden et al. (2022) cross-matched with our MW component sub-samples. Hayden et al. (2022) determined ages for GALAH DR3 stars using the XGBoost algorithm and a large range of chemical abundances, training the algorithm on isochronal ages for main sequence turn-off stars determined by Sharma et al. (2018). For our sample of GCs, we adopt isochronal ages from the study of VandenBerg et al. (2013), noting the consistent use of isochronal ages for both field stars and GCs.

Field star and GC ages are presented in Fig. 6. The mean Hayden et al. (2022) ages for both *in situ* halo and high- α disc stars, using 0.2 dex-sized bins in $[\text{Fe}/\text{H}]_{\text{K}20}$ are shown alongside the mean evolution of $[\text{O}/\text{Fe}]_{\text{K}20}$ versus $[\text{Fe}/\text{H}]_{\text{K}20}$. Because Hayden et al. (2022) do not derive ages for stars below $[\text{Fe}/\text{H}] = -1$, the oldest mean age in our high- α disc sample is coincidentally the average upper limit on the NIRVANDELS ages (11.7 Gyr). The location of the high- α disc (*in situ* halo) in $[\text{O}/\text{Fe}]_{\text{K}20}$ versus $[\text{Fe}/\text{H}]_{\text{K}20}$ at 11.7 Gyr is marked with a white star (white square). GCE models for the MW thick disc and bulge from K20 are also marked in Fig. 6 as the filled line and dashed line, respectively. When our high- α disc sample transitions to younger ages, showing stronger disagreement with the GCE model, we are likely dominated by contamination from

younger, low- α disc stars which have made it into our high- α disc sample (around $[\text{Fe}/\text{H}]_{\text{K}20} \sim -0.5$).

6.2 The Milky Way and GSE at $z \sim 3$

Using the field star and GC ages, we now attempt to project the MW and GSE back in time to $z \sim 3$ (11.7 Gyr look back time) to the era of the NIRVANDELS galaxies. Beginning with the *in situ* GC ages, selecting only GCs with an isochronal ages between 11–12 Gyr, we place the MW somewhere in the range of $-1.3 \leq [\text{Fe}/\text{H}]_{\text{K}20} \leq -0.7$ at $z \sim 3$. This range is marked with the shaded black region in Fig. 6 and reflects the average metallicity and standard deviation of the subset of *in situ* GCs. Field star ages from Hayden et al. (2022) support this placement, with an average binned age of 11.69 Gyr in the high- α disc and inner halo occurring at $[\text{Fe}/\text{H}]_{\text{K}20} = -0.95$ and $[\text{Fe}/\text{H}]_{\text{K}20} = -1.06$, respectively (marked as the white star and white square in Fig. 6, respectively).

In the case of GSE, only two GSE-tagged GCs in our sample have ages in the range of $z \sim 3$ (NGC 2808 and NGC 5904) in our combined Carretta et al. (2009)–VandenBerg et al. (2013) catalogue. These two GCs have isochronal ages of 11.0 and 11.5 Gyr, respectively, making the placement of the GSE point in $[\text{O}/\text{Fe}]_{\text{K}20}$ ($[\text{Fe}/\text{H}]_{\text{K}20}$) a lower (upper) limit. The range of metallicity spanned by these two GCs is $-1.4 \leq [\text{Fe}/\text{H}]_{\text{K}20} \leq -1.0$ marked with the cyan shaded region.

To estimate the location of the MW in $[\text{Fe}/\text{H}]_{\text{K}20}$ and $[\text{O}/\text{Fe}]_{\text{K}20}$ at $z \sim 3$, we average the $[\text{Fe}/\text{H}]_{\text{K}20}$ and $[\text{O}/\text{Fe}]_{\text{K}20}$ values from the *in situ* clusters with ages between 11–12 Gyr and do the same with the two

GSE-tagged GCs to estimate a location for GSE. Our final estimated values are $([\text{Fe}/\text{H}]_{\text{K20}}, [\text{O}/\text{Fe}]_{\text{K20}}) = (-1.04 \pm 0.33, 0.55 \pm 0.18)$ for the MW and $([\text{Fe}/\text{H}]_{\text{K20}}, [\text{O}/\text{Fe}]_{\text{K20}}) = (-1.20 \pm 0.13, 0.45 \pm 0.16)$ for the GSE at $z \sim 3$, where the uncertainty is the standard deviation for the set of GCs added in quadrature with the average individual GC measurement uncertainty and the shift applied to bring the GCs into agreement with A19 on the K20 scale (+0.15 dex, see Section 3.3).

Given the difficulty in deriving ages for metal-poor stars ($[\text{Fe}/\text{H}] < -1$; see Alencastro Puls et al. 2022, for a discussion of the complications in deriving astroseismic ages at the star-by-star level), we have limited data sets to compare against for our placement of GSE and the MW in $[\text{Fe}/\text{H}]_{\text{K20}}, [\text{O}/\text{Fe}]_{\text{K20}}$ at $z \sim 3$. We can compare the location of our GSE data points against the recent results of Horta et al. (2024) who select likely GSE members from the catalogue of MSTO-isochronal ages of Xiang & Rix (2022). Horta et al. (2024) find an average age of $11.6^{+1.14}_{-1.15}$ Gyr for their GSE sample across a metallicity range of $-2 \leq [\text{Fe}/\text{H}] \leq -1$. This range reinforces the likelihood that our placement of GSE at $[\text{Fe}/\text{H}]_{\text{K20}} = -1.2$ at $z \sim 3$ represents an upper limit on the location of GSE (it was likely less evolved than this at that time).

Another recent study examining the ages of accreted MW stars using both astroseismology and isochrones was performed by de Brito Silva et al. (2024). Examining their accreted stars with $[\text{Fe}/\text{H}] < -1$, and neglecting a single outlier with an astroseismic age of 6.5 Gyr, they find an average astroseismic age of 11.4 Gyr at $[\text{Fe}/\text{H}] = -1.24$ – in good agreement with our placement based on accreted GCs, but again suggesting that we are overestimating the location of GSE in $[\text{Fe}/\text{H}]_{\text{K20}}$ at $z \sim 3$.

Comparing our placement of the MW in $[\text{Fe}/\text{H}]_{\text{K20}}, [\text{O}/\text{Fe}]_{\text{K20}}$ at $z \sim 3$ with literature results, we find good agreement with the study of Queiroz et al. (2023) who derive MSTO-isochronal ages for the high- α disc using their STARHORSE code and multiple surveys (see their fig. 11, where 11 Gyr old stars show a mean metallicity of $[\text{Fe}/\text{H}] \approx -1$ in the LAMOST DR7, APOGEE DR17, and GALAH DR3 surveys). The results of Silva Aguirre et al. (2018) using the APOKASC catalogue (Pinsonneault et al. 2014) to derive ages for the high- α and low- α discs, also qualitatively agrees with our placement of the MW in $[\text{Fe}/\text{H}]_{\text{K20}}, [\text{O}/\text{Fe}]_{\text{K20}}$, though they do not age-date stars with $[\text{Fe}/\text{H}] < -1$ as their sample of high- α disc stars truncates around $[\text{Fe}/\text{H}] = -0.9$ [on the APOGEE scale, who in-turn adopt the abundances of Grevesse, Asplund & Sauval (2007) where $A(\text{Fe}) = 7.45$, 0.05 dex lower than the K20 scale]. In the range of $-0.9 \leq [\text{Fe}/\text{H}] \leq +0.4$, they find an average astroseismic age of 11 Gyr for the high- α disc, with ages generally increasing with decreasing metallicity (see their fig. 10).

6.3 The $z \sim 3$ mass–metallicity relation

Using our estimate of the position of the MW and GSE in $[\text{O}/\text{Fe}]_{\text{K20}}, [\text{Fe}/\text{H}]_{\text{K20}}$ at $z \sim 3$, we aim to place the two galaxies on the mass–metallicity relation (or MZR) for the NIRVANDELS galaxies recovered in Stanton et al. (2024). The MZR was first observed in local galaxies (e.g. McClure & van den Bergh 1968; Sandage 1972; Maiolino & Mannucci 2019, see the final reference for a more complete review of the subject). Very broadly, the physical cause of the relationship between increasing galactic mass and increasing metallicity is likely due to the shallower potential of low-mass galaxies, which allows SN-driven winds to more efficiently eject their metal-enriched gas (see Sharda et al. 2021a, b, for a recent and more detailed model capturing the many physical mechanisms driving the MZR).

The MZR appears to apply to both quiescent and SFGs, with different slopes. Its existence has been confirmed for the gas-phase ($Z_{\text{gas}}, [\text{O}/\text{H}]$ and $[\text{N}/\text{H}]$) metallicity out to $z \sim 3.5$ (e.g. Steidel et al. 2014; Onodera et al. 2016; Cullen et al. 2021; Sanders et al. 2021b; Strom et al. 2022; Stanton et al. 2024), with *JWST* surveys providing initial measurements out to $z \sim 10$ (e.g. Nakajima et al. 2023; Chemerynska et al. 2024; Curti et al. 2024). The stellar ($Z_*, [\text{Fe}/\text{H}]$) metallicity MZR has been measured out to $z < 5$ (e.g. Cullen et al. 2019; Kashino et al. 2022; Strom et al. 2022; Chartab et al. 2024; Stanton et al. 2024). The common slopes but differing normalizations for Z_{gas} and Z_* MZRs reflect the different nucleosynthetic channels responsible for forming oxygen and iron, providing further evidence for α -enhancement in high- z systems (Cullen et al. 2021; Strom et al. 2022; Stanton et al. 2024).

To assign an estimate for the mass of the MW and GSE at $z \sim 3$, we utilize results from the recent study of Kurbatov et al. (2024). They determine the density profiles for two ancient MW components, ‘Aurora’ (what we refer to as the ‘inner halo’; Belokurov & Kravtsov 2022) and GSE. In the case of GSE, we adopt the results from Kurbatov et al. (2024) assuming the exponentially truncated single power-law density profile for the spatial distribution of GSE from Lane et al. (2023). Kurbatov et al. (2024) provide estimates of the total stellar mass for each component as a function of metallicity (in the range of $-3 \leq [\text{Fe}/\text{H}] \leq -1$ using metallicities for Gaia RGB stars from Andrae, Rix & Chandra 2023). Using our estimates of the location of both the MW and GSE at $z \sim 3$ in $[\text{Fe}/\text{H}]$, we adopt a mass of $4.52 \times 10^8 M_{\odot}$ for Aurora (integrating up until $[\text{Fe}/\text{H}] = -1$) and $1.05 \pm 0.24 \times 10^8 M_{\odot}$ for GSE (averaging the total integrated mass between $-3 \leq [\text{Fe}/\text{H}] \leq -1.3$ and $-3 \leq [\text{Fe}/\text{H}] \leq -1.0$). Note that Kurbatov et al. (2024) does not quote uncertainties on their mass estimates.

Because the GCs we use to place GSE in $([\text{O}/\text{Fe}]_{\text{K20}}, [\text{Fe}/\text{H}]_{\text{K20}})$ have an average age (11.25 Gyr) less than our desired lookback time (11.7 Gyr), our positioning of GSE is likely an overestimate of how evolved the galaxy was at $z \sim 3$. To explore by how much we have overestimated the mass for the GSE, we turn to two studies which predict the SFHs of GSE using GCE modelling. Looking first at the study of Sanders, Belokurov & Man (2021a), they derive a SFH for GSE using data from APOGEE DR16 (Ahumada et al. 2020), GALAH DR3, and Nissen & Schuster (2010) and a bespoke GCE model. In the range of 11.7–11.25 Gyr, Sanders et al. (2021a) place GSE at the peak of its SF. Because of this, their results indicate GSE is approximately 2–3 times smaller at $z \sim 3$ than our estimate. The other study we compare to is Hasselquist et al. (2021), who derive SFH for GSE using APOGEE DR16 data and two GCE models. In the SFH derived by Hasselquist et al. (2021) using the `flexCE` (Andrews et al. 2017) GCE model, between 11.7–11.25 Gyr GSE is only moderately SF, with the peak occurring later at ~ 9 Gyr (consistent with the second age peak seen in Horta et al. 2024). Based on this, GSE was only 1.1 times more massive at 11.25 Gyr than it was at $z \sim 3$.

As shown in Fig. 6 using vertical lines, the appearance of coherent rotation and the emergence of the high- α disc (‘spin-up’) begin around $[\text{Fe}/\text{H}] = -1.3$ and is complete by $[\text{Fe}/\text{H}] > -0.9$ (determined using field star kinematics and chemical abundances; Belokurov & Kravtsov 2022). Note that the ‘spin-up’ phase may have begun even earlier than $[\text{Fe}/\text{H}] = -1.3$ based on recent results from Viswanathan et al. (2024). Regardless, our estimate of the $z \sim 3$ MW at $[\text{Fe}/\text{H}]_{\text{K20}} = -0.98$ based on field star and GC ages places the Galaxy slightly before the end of the primary disc-building phase—meaning that some high- α disc is present in our inner halo, or Aurora, sample. However, because Kurbatov et al. (2024) do not define their

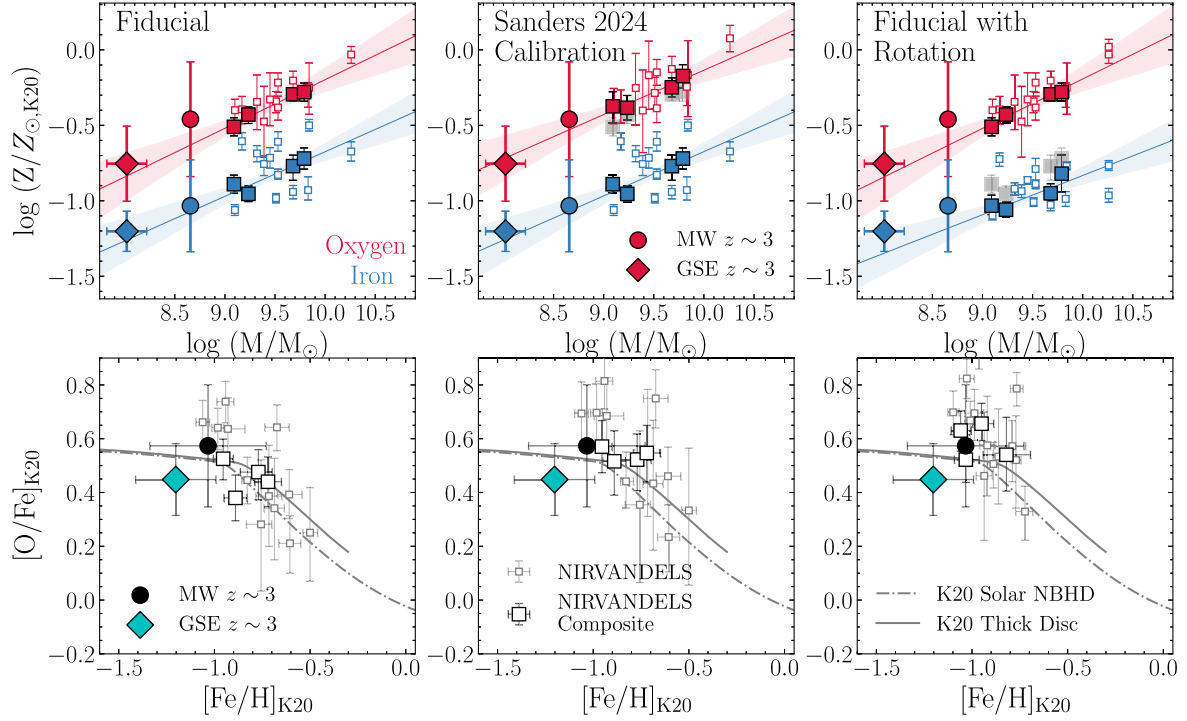


Figure 7. Results of projecting the MW (primarily the inner halo or ‘Aurora’) and GSE to $z \sim 3$. *Top*: metallicity–mass relation (MZR) using Z_{gas} (oxygen abundance, red) and Z_* (iron abundance, blue) for the NIRVANDELS sample of individual galaxies (small points) and composites (larger points). The MW and GSE are marked with the circle and diamond, respectively. *Bottom*: individual and composite NIRVANDELS galaxies in $[\text{O}/\text{Fe}]$ versus $[\text{Fe}/\text{H}]$ alongside the projected location of the MW (black circle) and GSE (teal diamond). The three columns reflect different methodologies to extract the galaxy abundances. In the first and last columns, Z_{gas} is determined using the Bian et al. (2018) strong-line calibration scheme, while in the middle column Z_{gas} is determined using the calibration scheme of Sanders et al. (2024). While all three columns derive Z_* using S99 models, the left and middle column use S99 models with no rotation, whilst the right column uses models including rotation. The location of the NIRVANDELS stacks in O and Fe determined using the fiducial calibration scheme (left-most column) are included in the middle and right-most columns (as grey points) to highlight the impact of different calibration schemes. **Note the remarkable consistency of the MW and GSE at $z \sim 3$ with predictions for the evolution of the gas (oxygen)- and stellar (iron) MZR from NIRVANDELS (top row) and the sensitivity of the NIRVANDELS abundances to the choice of calibration scheme (the shift in the appearance of a decreasing trend in $[\text{O}/\text{Fe}]_{\text{K20}}$ versus $[\text{Fe}/\text{H}]_{\text{K20}}$ to the appearance of a plateau, across panels in the bottom row).**

components in velocity space, contributions from the *in situ* high- α disc up until $[\text{Fe}/\text{H}] < -1$ are accounted for in their estimate, and our adopted total mass of the inner halo. We do not consider the contribution of the MW bulge in our estimate of the *in situ* population of the MW at $z \sim 3$ because stellar age estimates are extremely limited for bulge stars, and the metallicity range of bulge stars with reliable estimates of ages greater than 11 Gyr spans 1.5 dex (Bensby et al. 2017; Joyce et al. 2023) making it difficult to pinpoint a single location in the MZR.

We present the oxygen- and iron-MZR derived from the NIRVANDELS galaxies in the top row of Fig. 7 alongside estimates for the location of MW and GSE at $z \sim 3$. The best-fitting trends from Stanton et al. (2024) determined from the NIRVANDELS composite spectra (large squares) are shown for both the oxygen- (red) and iron-MZR (blue). Our estimated positions for the MW and GSE on the MZR are marked with a circle and diamond, respectively. Remarkably, the stellar-based oxygen abundances and iron metallicities of both the MW and GSE seem to follow the low mass extrapolation of the corresponding relations obtained by Stanton et al. (2024) across the three different modelling techniques (shown across the three columns). Recent results for the $z = 3$ MZR from the THESAN-ZOOM (Kannan et al. 2025) simulations also show very good agreement with the NIRVANDELS MZR and our MW and GSE data points (McClymont+ in preparation). The oxygen-

and iron-MZRs in the first column are calculated using the using the fiducial strong-line calibrated scheme and stellar models described in Section 4.1, the middle column is calculated using the same stellar models but applies the *JWST*-based calibration scheme of Sanders et al. (2024), while the right-most column uses the fiducial oxygen abundances but incorporates S99 models with rotation.

The effects of these different approaches were discussed in Section 4.4 and the bottom row of Fig. 7 illustrates the impact on the location of the NIRVANDELS data points in $[\text{O}/\text{Fe}]_{\text{K20}}$ versus $[\text{Fe}/\text{H}]_{\text{K20}}$. Adopting the *JWST*-based strong-line diagnostics from Sanders et al. (2024) increases the gas-phase O/H by ~ 0.1 dex (centre panels), shifting the $z \sim 3$ galaxies above the K20 relation, MW and GSE, in line with expectations of the NIRVANDELS galaxies being more greatly oxygen-enhanced than the MW at similar epochs. Including stellar rotation has the same overall effect by decreasing the stellar Fe/H by ~ 0.1 dex (right panels). We note that stellar population models that take into account the presence of binary stars (BPASS; Eldridge & Stanway 2016; Stanway et al. 2016; Stanway & Eldridge 2018) have a similar systematic effect on the derived Fe abundances as the use of single-star models with rotation (i.e. it typically leads to lower Fe abundances than those derived using S99 models without rotation, thereby shifting high- z galaxies up and to the left in the $[\text{O}/\text{Fe}]-[\text{Fe}/\text{H}]$ diagram, e.g. Chisholm et al. 2019; Cullen et al. 2019, 2021).

The position of the MW and GSE on the star-forming NIRVANDELS MZR suggests that both galaxies were actively star-forming at $z \sim 3$. Given the metallicity distributions of both galaxies, they were likely star forming at even earlier times. It is possible that they were among the low-mass, SFGs which could have reionized the Universe. In their recent study examining 677 galaxies across $z = 4\text{--}7$ in the mass range of $\log(M_*/M_\odot) = 7\text{--}10$ (less massive than both the MW and GSE at $z \sim 3$), Simmonds et al. (2024) find an increasing trend of ionizing photon production efficiency with decreasing galaxy UV brightness and stellar mass (see also Begley et al. 2025). They conclude that, if their sample is representative of faint, low mass, bursty SFGs, these galaxies are efficient enough to reionize the Universe. Given that Simmonds et al. (2024) were able to observe $10^7 M_\odot$ galaxies at $z > 4$ and given our estimated masses for GSE and the MW ($> 10^7 M_\odot$ at $z \sim 3$), it is possible that *JWST* is currently observing GSE and MW analogues in the early Universe, an exciting prospect for the placement of our Local Universe in the broader context of global galaxy evolution.

7 CONCLUSIONS

With the shared goal of understanding the chemical evolution of all galaxies including our own, we founded the ChemZz collaboration to couple results from extragalactic and Galactic chemical abundance studies. In this first study, we placed oxygen and iron measurements made from evolved stars in the MW, Local Group galaxies, and GCs on to the same scale as those made in star forming regions in unresolved galaxies at Cosmic Noon ($z \sim 2\text{--}3$). To do this, we reviewed the assumptions relevant to the methods in both samples and the systematics affecting each.

Abundances for the MW were taken from the third data release of the GALAH survey (Buder et al. 2021), splitting the MW into four chemodynamic components, namely the high- α (thick) and low- α (thin) discs and inner and outer halo, the latter we assume to be dominated by debris from the GSE merger (Belokurov et al. 2018; Helmi et al. 2018) using various chemical and kinematic cuts. Abundances from the O-normal, first population, stars in MW GCs were also included, taken from the study of Carretta et al. (2009). After bringing the MW and GC data on to the K20 scale and considering their kinematic associations, we applied small shifts to bring them into agreement with the study of Amarsi et al. (2019) on the Kobayashi et al. (2020b, K20) scale, which we adopt as our ground truth abundances. We also compiled abundance measurements for evolved stars in the LMC (Pompéia et al. 2008; Van der Swaelmen et al. 2013), SMC (Mucciarelli et al. 2023), and Sgr (Carretta et al. 2010) dwarf galaxies and measurements derived from PNe in M 31 (Bhattacharya et al. 2022).

Extragalactic O and Fe abundances were collated from three main surveys, the KBSS (Rudie et al. 2012; Steidel et al. 2014), the LATIS (Chartab et al. 2024) and the NIRVANDELS survey (Cullen et al. 2021; Stanton et al. 2024). In the case of LATIS, we adopt the stacked measurement (derived from composite spectra created by combining all individual galaxies in the survey) only, in KBSS we include both the stacked measurement from Steidel et al. (2016) and representative points from the mass–metallicity relations derived by Strom et al. (2022), and in NIRVANDELS we include both the stacked and individual galaxy abundances. All abundances were corrected for depletion on to dust and brought on to the K20 scale.

After bringing all of our data sets to a common scale, we compare resolved stellar abundance measurements of oxygen and iron in Local Group galaxies and star clusters, with gas-phase and stellar

metallicities in galaxies at Cosmic Noon via the Tinsley–Wallerstein diagram (Wallerstein 1962; Tinsley 1979).

The main takeaways from this study are as follows:

(i) We find that stacked abundances from the LATIS (Chartab et al. 2024) and KBSS surveys (Steidel et al. 2016; Strom et al. 2022) show clear O-enhancement in agreement with the MW high- α disc and inner halo, while individual massive, SFGs from NIRVANDELS (Cullen et al. 2021; Stanton et al. 2024) show increased diversity of $[\text{O}/\text{Fe}]_{\text{K20}}$ abundances, agreeing with both the high- α and low- α discs (left panels of Fig. 5).

(ii) When placed on to a common abundance scale, we find excellent agreement in $[\text{O}/\text{Fe}]_{\text{K20}}$ versus $[\text{Fe}/\text{H}]_{\text{K20}}$ between the MW high- α (thick) and low- α (thin) discs and old α -rich, and young α -poor, PNe in M 31, supporting the existence of an α -bimodality in the inner regions of the disc of M 31 (left panels of Fig. 5).

(iii) Using ages for GCs associated with the *in situ* MW and accreted halo (assumed to be dominated by the GSE), we estimate the location of the MW and GSE in $[\text{O}/\text{Fe}]_{\text{K20}}$ versus $[\text{Fe}/\text{H}]_{\text{K20}}$ at $z \sim 3$, or a look back time of 11.7 Gyr (Fig. 6). Our final estimated values are $([\text{Fe}/\text{H}]_{\text{K20}}, [\text{O}/\text{Fe}]_{\text{K20}}) = (-1.04 \pm 0.33, 0.55 \pm 0.18)$ for the MW and $([\text{Fe}/\text{H}]_{\text{K20}}, [\text{O}/\text{Fe}]_{\text{K20}}) = (-1.20 \pm 0.13, 0.45 \pm 0.16)$ for the GSE.

(iv) After re-scaling, and independent of the calibration scheme, some NIRVANDELS galaxies appear more $[\text{O}/\text{Fe}]_{\text{K20}}$ -poor than the less massive MW at $z \sim 3$ (bottom panels of Fig. 7), implying the existence of stars that were formed after Type Ia SNe had contributed a significant amount of Fe. This likely reflects a diversity of star formation histories that may include already declining star formation or an early episode of star formation followed by additional bursts (e.g. as in the bursty models of Kobayashi & Ferrara 2024).

(v) Combining our estimate of the location of the MW and GSE in $[\text{O}/\text{Fe}]_{\text{K20}}$ and $[\text{Fe}/\text{H}]_{\text{K20}}$ at $z \sim 3$ with estimates of their masses at this time from Kurbatov et al. (2024), we plot the two on the O-, Fe-mass–metallicity relation of star-forming NIRVANDELS galaxies. We find excellent agreement between the location of the two galaxies and the predictions for the low-mass end of both the NIRVANDELS O- and Fe-mass–metallicity relations, independent of the abundance calibration scheme (top panels of Fig. 7).

In the future, we will investigate the abundance of carbon and nitrogen across the Local Group and at Cosmic Noon and include measurements of the kinematics of our Cosmic Noon sample to understand the relationship between chemical evolution and the emergence of galactic discs. Additionally, a larger set of homogeneous GC isochronal ages from projects like CARMA (Massari et al. 2023) will greatly aid with attempts to project both the MW and GSE further back in time in abundance space. Upcoming large scale surveys measuring homogeneous NLTE-corrected oxygen abundances for millions of stars throughout the MW, like WEAVE (Dalton et al. 2012) and 4MOST (de Jong et al. 2012), will greatly aid studies like ours. Further studies like ours and that of Ji et al. (2025) and Chruślińska et al. (2024), working to compare resolved stellar abundances directly to stellar- and gas-phase abundances and metallicities across redshifts will continue to test the compatibility of these distinct abundance derivation techniques. In parallel, harnessing techniques like those of Lian et al. (2023), which translate resolved stellar abundances in the MW to integrated light measurements will allow for more direct comparisons between Local Group galaxies and extragalactic abundances. Moreover, integral-field spectrographs on the ELTs will allow us to spatially resolve low-mass galaxies at Cosmic Noon (Newman et al. 2019), enabling novel connections between distinct components of MW progenitor

analogues and our own Galaxy. In all of these efforts, we emphasize the need for increased transparency around the choice of solar scale and abundance methodology, in order to maximize the scientific return of studies attempting to couple extragalactic and Galactic chemical abundances.

ACKNOWLEDGEMENTS

The authors warmly thank the referee for their helpful comments and suggestions that greatly improved this paper. The ChemZz collaboration is incredibly grateful to the organizers and support staff of the Lorentz Center workshop ‘Gravitational waves: a new ear on the chemistry of galaxies’, where the idea for this paper was born. SM thanks Magda Arnaboldi for her very helpful feedback and Vasily Belokurov for discussions which helped progress this project. TMS and FC acknowledge support from a UK Research and Innovations UKRI Frontier Research Guarantee Grant (PI Cullen; grant reference: EP/X021025/1). JLS acknowledges support from the Royal Society (URF\R1\191555). CK acknowledges funding from the UK Science and Technology Facility Council through grant ST/Y001443/1. TS gratefully acknowledges the support of the NSF-Simons AI-Institute for the Sky (SkAI) via grants NSF AST-2421845 and Simons Foundation MPS-AI-00010513 and of NASA grants 22-ROMAN22-0055 and 22-ROMAN22-0013. This work relies heavily on the ASTROPY (Astropy Collaboration 2013, 2018), SCIPY (Virtanen et al. 2020), NUMPY (Harris et al. 2020), and MATPLOTLIB (Hunter 2007) libraries and JUPYTER notebooks (Kluyver et al. 2016).

This work makes use of data from the GALAH survey, observed using the Anglo-Australian Telescope on the unceded territory of the Gamilaraay people. We acknowledge the traditional custodians of the land and pay our respects to elders past and present.

Some of the data presented herein were obtained at Keck Observatory, which is a private 501(c)3 non-profit organization operated as a scientific partnership among the California Institute of Technology, the University of California, and the National Aeronautics, and Space Administration. The Observatory was made possible by the generous financial support of the W. M. Keck Foundation. The authors also wish to recognise and acknowledge the very significant cultural role and reverence that the summit of Maunakea has always had within the Native Hawaiian community. We are most fortunate to have the opportunity to conduct observations from this mountain.

DATA AVAILABILITY

Data for the Cosmic Noon sample is included in Table 2. Abundances for the MW sample, Local Group, and M 31 are all already publicly available.

REFERENCES

- Abdurro’uf et al., 2022, *ApJS*, 259, 35
 Ahumada R. et al., 2020, *ApJS*, 249, 3
 Alencastro Puls A., Casagrande L., Monty S., Yong D., Liu F., Stello D., Aguirre Børsen-Koch V., Freeman K. C., 2022, *MNRAS*, 510, 1733
 Amarsi A. M. et al., 2020, *A&A*, 642, A62
 Amarsi A. M., Nissen P. E., Skúladóttir Á., 2019, *A&A*, 630, A104 (A19)
 Andrae R., Rix H.-W., Chandra V., 2023, *ApJS*, 267, 8
 Andrews B. H., Weinberg D. H., Schönrich R., Johnson J. A., 2017, *ApJ*, 835, 224
 Ardern-Arentsen A. et al., 2024, *MNRAS*, 530, 3391
 Arellano-Córdova K. Z. et al., 2022, *ApJ*, 940, L23
 Arnaboldi M. et al., 2022, *A&A*, 666, A109
 Asplund M., Amarsi A. M., Grevesse N., 2021, *A&A*, 653, A141
 Asplund M., Grevesse N., Sauval A. J., Scott P., 2009, *ARA&A*, 47, 481
 Astropy Collaboration, 2013, *A&A*, 558, A33
 Astropy Collaboration, 2018, *AJ*, 156, 123
 Astropy Collaboration, 2022, *ApJ*, 935, 167
 Baldwin J. A., Phillips M. M., Terlevich R., 1981, *PASP*, 93, 5
 Begley R. et al., 2025, *MNRAS*, 537, 3245
 Belokurov V., Erkal D., Evans N. W., Koposov S. E., Deason A. J., 2018, *MNRAS*, 478, 611
 Belokurov V., Kravtsov A., 2022, *MNRAS*, 514, 689
 Belokurov V., Kravtsov A., 2023, *MNRAS*, 525, 4456
 Belokurov V., Kravtsov A., 2024, *MNRAS*, 528, 3198
 Belokurov V., Sanders J. L., Fattahi A., Smith M. C., Deason A. J., Evans N. W., Grand R. J. J., 2020, *MNRAS*, 494, 3880
 Bensby T. et al., 2017, *A&A*, 605, A89
 Bensby T., Feltzing S., Lundström I., 2003, *A&A*, 410, 527
 Bensby T., Feltzing S., Oey M. S., 2014, *A&A*, 562, A71
 Besla G., 2015, preprint (arXiv:1511.03346)
 Bhattacharya S. et al., 2019b, *A&A*, 631, A56
 Bhattacharya S. et al., 2022, *MNRAS*, 517, 2343
 Bhattacharya S., Arnaboldi M., Gerhard O., Kobayashi C., Saha K., 2025, *ApJL*, 983, 2, 11
 Bhattacharya S., Arnaboldi M., Gerhard O., McConnachie A., Caldwell N., Hartke J., Freeman K. C., 2021, *A&A*, 647, A130
 Bhattacharya S., Arnaboldi M., Hammer F., Yang Y., Gerhard O., Caldwell N., Freeman K. C., 2023, *MNRAS*, 522, 6010
 Bhattacharya S., Arnaboldi M., Hartke J., Gerhard O., Comte V., McConnachie A., Caldwell N., 2019a, *A&A*, 624, A132
 Bhattacharya S., Arnaboldi M., Kobayashi C., Gerhard O., Saha K., 2025, preprint (arXiv:2505.01896)
 Bian F., Kewley L. J., Dopita M. A., 2018, *ApJ*, 859, 175
 Bland-Hawthorn J., Gerhard O., 2016, *ARA&A*, 54, 529
 Boardman N. et al., 2020, *MNRAS*, 491, 3672
 Bonaca A. et al., 2020, *ApJ*, 897, L18
 Bovy J., 2015, *ApJS*, 216, 29
 Bryant J. J. et al., 2015, *MNRAS*, 447, 2857
 Buder S. et al., 2021, *MNRAS*, 506, 150
 Buder S. et al., 2022, *MNRAS*, 510, 2407
 Buder S. et al., 2025, *PASA*, 42, 42
 Bundy K. et al., 2015, *ApJ*, 798, 7
 Bunker A. J. et al., 2023, *A&A*, 677, A88
 Burbidge E. M., Burbidge G. R., Fowler W. A., Hoyle F., 1957, *Rev. Mod. Phys.*, 29, 547
 Carney B. W., Latham D. W., Laird J. B., 1988, *AJ*, 96, 560
 Carniani S. et al., 2025, *A&A*, 696, 14
 Carollo D. et al., 2007, *Nature*, 450, 1020
 Carretta E. et al., 2010, *A&A*, 520, A95
 Carretta E., Bragaglia A., Gratton R., Lucatello S., 2009, *A&A*, 505, 139
 Carrillo A., Hawkins K., Jofré P., de Brito Silva D., Das P., Lucey M., 2022, *MNRAS*, 513, 1557
 Castellano M. et al., 2024, *ApJ*, 972, 143
 Ceccarelli E., Mucciarelli A., Massari D., Bellazzini M., Matsuno T., 2025, preprint arXiv:2503.02939
 Chabrier G., 2003, *PASP*, 115, 763
 Charbonnel C., Schaerer D., Prantzos N., Ramírez-Galeano L., Fragos T., Kuruvanthodi A., Marques-Chaves R., Gieles M., 2023, *A&A*, 673, L7
 Chartab N., Newman A. B., Rudie G. C., Blanc G. A., Kelson D. D., 2024, *ApJ*, 960, 73
 Chemerynska I. et al., 2024, *ApJL*, 976, 1, 11
 Chen B., Ting Y.-S., Hayden M., 2024, *PASA*, 41, e063
 Chen Y. et al., 2023, *Nat. Astron.*, 7, 771
 Chisholm J., Rigby J. R., Bayliss M., Berg D. A., Dahle H., Gladders M., Sharon K., 2019, *ApJ*, 882, 182
 Chruslińska M., Pakmor R., Matthee J., Matsuno T., 2024, *A&A*, 686, A186
 Ciucă I. et al., 2024, *MNRAS*, 528, L122
 Côté B., O’Shea B. W., Ritter C., Herwig F., Venn K. A., 2017, *ApJ*, 835, 128
 Croxall K. V. et al., 2013, *ApJ*, 777, 96
 Cui X.-Q. et al., 2012, *Res. Astron. Astrophys.*, 12, 1197
 Cullen F. et al., 2019, *MNRAS*, 487, 2038

- Cullen F. et al., 2021, *MNRAS*, 505, 903
- Curti M. et al., 2024, *A&A*, 684, A75
- D'Antona F. et al., 2023, *A&A*, 680, L19
- D'Souza R., Bell E. F., 2018, *Nat. Astron.*, 2, 737
- Dalton G. et al., 2012, in McLean I. S., Ramsay S. K., Takami H., eds, Proc. SPIE Conf. Ser. Vol. 8446, Ground-based and Airborne Instrumentation for Astronomy IV. SPIE, Bellingham, p. 84460P
- Davies E. Y., Belokurov V., Kravtsov A., Monty S., Myeong G., Evans N. W., Kane S. G., 2025, *MNRAS*, 539, 2
- de Boer T. J. L., Belokurov V., Koposov S., 2015, *MNRAS*, 451, 3489
- de Brito Silva D., Jofré P., Worley C., Hawkins K., Das P., 2024, *A&A*, 690, A120
- de Jong R. S. et al., 2012, in McLean I. S., Ramsay S. K., Takami H., eds, Proc. SPIE Conf. Ser. Vol. 8446, Ground-based and Airborne Instrumentation for Astronomy IV. SPIE, Bellingham, p. 84460T
- de los Reyes M., Besla G., Oey M., 2024, American Astronomical Society Meeting Abstracts. p. 118.05
- De Silva G. M. et al., 2015, *MNRAS*, 449, 2604
- Deason A. J., Belokurov V., 2024, *New Astron. Rev.*, 99, 101706
- Dessauges-Zavadsky M., D'Odorico S., Schaerer D., Modigliani A., Tapken C., Vernet J., 2010, *A&A*, 510, A26
- Dey A. et al., 2023, *ApJ*, 944, 1
- Dorman Claire E., Guhathakurta Puragra, Seth Anil C., Weisz Daniel R., Bell Eric F., Dalcanton Julianne J., Gilbert Karoline M., Hamren Katherine M., Lewis Alexia R., Skillman Evan D., Toloba Elisa, Williams Benjamin F., 2015, *The Astrophysical Journal*, 803, 24
- Dressler A. et al., 2011, *PASP*, 123, 288
- Eldridge J. J., Stanway E. R., 2016, *MNRAS*, 462, 3302
- Fattahi A. et al., 2019, *MNRAS*, 484, 4471
- Ferland G. J. et al., 2013, *Rev. Mex. Astron. Astrofis.*, 49, 137
- Feuillet D. K., Feltzing S., Sahlholdt C. L., Casagrande L., 2020, *MNRAS*, 497, 109
- Foster C. et al., 2021, *Publ. Astron. Soc. Aust.*, 38, e031
- Fraser-McKelvie A., Merrifield M., Aragón-Salamanca A., 2019, *MNRAS*, 489, 5030
- Freeman K., Bland-Hawthorn J., 2002, *ARA&A*, 40, 487
- Fuhrmann K., 1998, *A&A*, 338, 161
- Gaia Collaboration, 2016, *A&A*, 595, A2
- Gaia Collaboration, 2018, *A&A*, 616, A1
- Gaia Collaboration, 2023, *A&A*, 674, A1
- García-Rojas J., Esteban C., 2007, *ApJ*, 670, 457
- Garilli B. et al., 2021, *A&A*, 647, A150
- Gilmore G. et al., 2012, *The Messenger*, 147, 25
- Gilmore G., Wyse R. F. G., 1985, *AJ*, 90, 2015
- Gilmore G., Wyse R. F. G., Jones J. B., 1995, *AJ*, 109, 1095
- Grand R. J. J. et al., 2021, *MNRAS*, 507, 4953
- Gratton R. G., Carretta E., Claudi R., Lucatello S., Barbieri M., 2003, *A&A*, 404, 187
- Gratton R., Sneden C., Carretta E., 2004, *ARA&A*, 42, 385
- Grevesse N., Asplund M., Sauval A. J., 2007, *Space Sci. Rev.*, 130, 105
- Gustafsson B., Edvardsson B., Eriksson K., Jørgensen U. G., Nordlund Å., Plez B., 2008, *A&A*, 486, 951
- Halliday C. et al., 2008, *A&A*, 479, 417
- Hammer F., Yang Y. B., Wang J. L., Ibata R., Flores H., Puech M., 2018, *MNRAS*, 475, 2754
- Harris C. R. et al., 2020, *Nature*, 585, 357
- Hasselquist S. et al., 2021, *ApJ*, 923, 172
- Hayden M. R. et al., 2014, *AJ*, 147, 116
- Hayden M. R. et al., 2015, *ApJ*, 808, 132
- Hayden M. R. et al., 2022, *MNRAS*, 517, 5325
- Haywood M., Di Matteo P., Lehnert M. D., Snaith O., Khoperskov S., Gómez A., 2018, *ApJ*, 863, 113
- Helfer H. L., Wallerstein G., Greenstein J. L., 1959, *ApJ*, 129, 700
- Helmi A., 2020, *ARA&A*, 58, 205
- Helmi A., Babusiaux C., Koppelman H. H., Massari D., Veljanoski J., Brown A. G. A., 2018, *Nature*, 563, 85
- Horta D. et al., 2020, *MNRAS*, 493, 3363
- Horta D., Lu Y. L., Ness M. K., Lisanti M., Price-Whelan A. M., 2024, *ApJ*, 971, 170
- Hunt J. A. S., Vasiliev E., 2025, *New Astronomy Reviews*, 100
- Hunter J. D., 2007, *Comput. Sci. Eng.*, 9, 90
- Ji X. et al., 2025, *MNRAS*, 541, 3, 2134
- Ji X., Belokurov V., Maiolino R., Monty S., Isobe Y., Kravtsov A., McClymont W., Übler H., 2025, preprint (arXiv:2505.12505)
- Johnson C. I., Rich R. M., Kobayashi C., Kunder A., Koch A., 2014, *AJ*, 148, 67
- Johnson J. W. et al., 2021, *MNRAS*, 508, 4484
- Jönsson H. et al., 2020, *AJ*, 160, 120
- Joyce M., Johnson C. I., Marchetti T., Rich R. M., Simion I., Bourke J., 2023, *ApJ*, 946, 28
- Jurić M. et al., 2008, *ApJ*, 673, 864
- Kannan R. et al., 2025, preprint (arXiv:2502.20437)
- Kashino D. et al., 2022, *ApJ*, 925, 82
- Kennicutt R. C., Jr, 1998, *ApJ*, 498, 541
- Kewley L. J., Ellison S. L., 2008, *ApJ*, 681, 1183
- Kewley L. J., Nicholls D. C., Sutherland R. S., 2019, *ARA&A*, 57, 511
- Kluyver T. et al., 2016, in Loizides F., Schmidt B., eds, Positioning and Power in Academic Publishing: Players, Agents and Agendas. p. 87, IOS Press BV, Amsterdam, Netherlands
- Kobayashi C., Bhattacharya S., Arnaboldi M., Gerhard O., 2023, *ApJ*, 956, L14
- Kobayashi C., Ferrara A., 2024, *ApJ*, 962, L6
- Kobayashi C., Karakas A. I., Lugaro M., 2020b, *ApJ*, 900, 179 (K20)
- Kobayashi C., Leung S.-C., Nomoto K., 2020a, *ApJ*, 895, 138
- Kobayashi C., Nakasato N., 2011, *ApJ*, 729, 16
- Kobayashi C., Umeda H., Nomoto K., Tominaga N., Ohkubo T., 2006, *ApJ*, 653, 1145
- Kos J. et al., 2025, preprint (arXiv:2501.06140)
- Kriek M. et al., 2015, *ApJS*, 218, 15
- Kurbatov E. P. et al., 2024, preprint (arXiv:2410.22250)
- Lane J. M. M., Bovy J., Mackereth J. T., 2023, *MNRAS*, 526, 1209
- Laseter I. H. et al., 2024, *A&A*, 681, A70
- Le Fèvre O. et al., 2003, in Iye M., Moorwood A. F. M., eds, Proc. SPIE Conf. Ser. Vol. 4841, Instrument Design and Performance for Optical/Infrared Ground-based Telescopes. SPIE, Bellingham, p. 1670
- Legnardi M. V. et al., 2022, *MNRAS*, 513, 735
- Leitherer C., Ekström S., Meynet G., Schaerer D., Agienko K. B., Levesque E. M., 2014, *ApJS*, 212, 14
- Leitherer C., Ortiz Otálvaro P. A., Bresolin F., Kudritzki R.-P., Lo Faro B., Pauldrach A. W. A., Pettini M., Rix S. A., 2010, *ApJS*, 189, 309
- Lewis I. J. et al., 2002, *MNRAS*, 333, 279
- Lian J., Bergemann M., Pillepich A., Zasowski G., Lane R. R., 2023, *Nat. Astron.*, 7, 951
- Licquia T. C., Newman J. A., 2015, *ApJ*, 806, 96
- Lind K., Bergemann M., Asplund M., 2012, *MNRAS*, 427, 50
- Lucey M. et al., 2021, *MNRAS*, 501, 5981
- Mackereth J. T. et al., 2019, *MNRAS*, 489, 176
- Mackey D. et al., 2019, *Nature*, 574, 69
- Maiolino R., Mannucci F., 2019, *A&AR*, 27, 3
- Mason A. C., Crain R. A., Schiavon R. P., Weinberg D. H., Pfeffer J., Schaye J., Schaller M., Theuns T., 2024, *MNRAS*, 533, 184
- Massari D. et al., 2023, *A&A*, 680, A20
- Massari D., Koppelman H. H., Helmi A., 2019, *A&A*, 630, L4
- Matsuno T., Amarsi A. M., Carlos M., Nissen P. E., 2024, *A&A*, 688, A72
- Matteucci F., 2021, *A&AR*, 29, 5
- Matteucci F., Greggio L., 1986, *A&A*, 154, 279
- McClure R. D., van den Bergh S., 1968, *AJ*, 73, 1008
- McKenzie M. et al., 2022, *MNRAS*, 516, 3515
- McKenzie M. et al., 2024, *MNRAS*, 534, L35
- McLean I. S. et al., 2012, in McLean I. S., Ramsay S. K., Takami H., eds, Proc. SPIE Conf. Ser. Vol. 8446, Ground-based and Airborne Instrumentation for Astronomy IV. SPIE, Bellingham, p. 84460J
- McLure R. J. et al., 2018, *MNRAS*, 479, 25
- McMillan P. J., 2017, *MNRAS*, 465, 76

- Méndez-Delgado J. E., Esteban C., García-Rojas J., Kreckel K., Peimbert M., 2023, *Nature*, 618, 249
- Merrett H. R., Merrifield M. R., Douglas N. G., Kuijken K., Romanowsky A. J., Iannicola G. R., Arnaboldi M., Capaccioli M., Freeman K. C., Gerhard O., Coccato L., Carter D., Evans N. W., Wilkinson M. I., Halliday C., Bridges T. J., 2006, *Monthly Notices of the Royal Astronomical Society*, 369, 120
- Mesa-Delgado A., Esteban C., García-Rojas J., 2008, *ApJ*, 675, 389
- Miglio A. et al., 2021, *A&A*, 645, A85
- Milone A. P., Marino A. F., 2022, *Universe*, 8, 359
- Minchev I., Chiappini C., Martig M., 2013, *A&A*, 558, A9
- Montalbán J. et al., 2021, *Nat. Astron.*, 5, 640
- Monty S. et al., 2023b, *MNRAS*, 522, 4404
- Monty S. et al., 2024, *MNRAS*, 533, 2, 2420
- Monty S., Venn K. A., Lane J. M. M., Lokhorst D., Yong D., 2020, *MNRAS*, 497, 1236
- Monty S., Yong D., Marino A. F., Karakas A. I., McKenzie M., Grundahl F., Mura-Guzmán A., 2023a, *MNRAS*, 518, 965
- Morishita T., Stiavelli M., Schuldt S., Grillo C., 2025, *ApJ*, 979, 87
- Mucciarelli A., Minelli A., Bellazzini M., Lardo C., Romano D., Origlia L., Ferraro F. R., 2023, *A&A*, 671, A124
- Myeong G. C., Belokurov V., Aguado D. S., Evans N. W., Caldwell N., Bradley J., 2022, *ApJ*, 938, 21
- Myeong G. C., Vasiliev E., Iorio G., Evans N. W., Belokurov V., 2019, *MNRAS*, 488, 1235
- Naidu R. P. et al., 2021, *ApJ*, 923, 92
- Naidu R. P. et al., 2025, preprint (arXiv:2505.11263)
- Nakajima K., Ouchi M., Ito Y., Harikane Y., Zhang Y., Ono Y., Umeda H., Oguri M., 2023, *ApJS*, 269, 2, 30
- Nakane M. et al., 2024, *ApJ*, 976, 122
- Nakane M. et al., 2025, preprint (arXiv:2503.11457)
- Ness M. et al., 2013, *MNRAS*, 430, 836
- Ness M., Freeman K., 2016, *Publ. Astron. Soc. Aust.*, 33, e022
- Newman A. et al., 2019, *BAAS*, 51, 145
- Nidever D. L. et al., 2020, *ApJ*, 895, 88
- Nidever D. L. et al., 2024, in Tabatabaei F., Barbuy B., Ting Y.-S., eds, *Proc. IAU Symp. 377, Early Disk-Galaxy Formation from JWST to the Milky Way*. p. 115
- Nissen P. E., Gustafsson B., 2018, *A&AR*, 26, 6
- Nissen P. E., Schuster W. J., 2010, *A&A*, 511, L10
- Oke J. B. et al., 1995, *PASP*, 107, 375
- Onodera M. et al., 2016, *ApJ*, 822, 42
- Peimbert A., Peimbert M., 2010, *ApJ*, 724, 791
- Peimbert M., 1967, *ApJ*, 150, 825
- Peña-Guerrero M. A., Peimbert A., Peimbert M., Ruiz M. T., 2012, *ApJ*, 746, 115
- Pentericci L. et al., 2018, *A&A*, 616, A174
- Pinsonneault M. H. et al., 2014, *ApJS*, 215, 19
- Piskunov N., Valenti J. A., 2017, *A&A*, 597, A16
- Pompéia L. et al., 2008, *A&A*, 480, 379
- Prochaska J. X., Naumov S. O., Carney B. W., McWilliam A., Wolfe A. M., 2000, *AJ*, 120, 2513
- Queiroz A. B. A. et al., 2023, *A&A*, 673, A155
- Reddy B. E., Lambert D. L., Allende Prieto C., 2006, *MNRAS*, 367, 1329
- Rix S. A., Pettini M., Leitherer C., Bresolin F., Kudritzki R.-P., Steidel C. C., 2004, *ApJ*, 615, 98
- Rogers N. S. J., Strom A. L., Rudie G. C., Trainor R. F., Raptis M., von Raesfeld C., 2024, *ApJ*, 964, L12
- Rudie G. C. et al., 2012, *ApJ*, 750, 67
- Sandage A., 1972, *ApJ*, 176, 21
- Sandage A., Fouts G., 1987, *AJ*, 93, 74
- Sanders J. L., Belokurov V., Man K. T. F., 2021a, *MNRAS*, 506, 4321
- Sanders R. L. et al., 2020, *MNRAS*, 491, 1427
- Sanders R. L. et al., 2021b, *ApJ*, 914, 19
- Sanders R. L., Shapley A. E., Topping M. W., Reddy N. A., Brammer G. B., 2024, *ApJ*, 962, 24
- Schmidt M., 1959, *ApJ*, 129, 243
- Scholte D. et al., 2025, *MNRAS*, 540, 2, 1800
- Schönrich R., Binney J., 2009, *MNRAS*, 396, 203
- Schönrich R., Binney J., Dehnen W., 2010, *MNRAS*, 403, 1829
- Scott N., van de Sande J., Sharma S., Bland-Hawthorn J., Freeman K., Gerhard O., Hayden M. R., McDermid R., 2021, *ApJ*, 913, L11
- Sharda P., Krumholz M. R., Wisnioski E., Acharyya A., Federrath C., Forbes J. C., 2021b, *MNRAS*, 504, 53
- Sharda P., Krumholz M. R., Wisnioski E., Forbes J. C., Federrath C., Acharyya A., 2021a, *MNRAS*, 502, 5935
- Sharma S. et al., 2018, *MNRAS*, 473, 2004
- Sharma S. et al., 2019, *MNRAS*, 490, 5335
- Sharma S., Hayden M. R., Bland-Hawthorn J., 2021, *MNRAS*, 507, 5882
- Sharples R. et al., 2013, *The Messenger*, 151, 21
- Sheinis A. et al., 2015, *J. Astron. Telesc. Instrum. Syst.*, 1, 035002
- Shipp N. et al., 2021, *ApJ*, 923, 149
- Silva Aguirre V. et al., 2018, *MNRAS*, 475, 5487
- Simmonds C. et al., 2024, *MNRAS*, 527, 6139
- Somawanshi D., Bhattacharya S., Kataria M., Kobayashi C., 2024, *MNRAS*, 531, 4336
- Somawanshi D., Bhattacharya S., Kataria M., Mishra P. K., Kobayashi C., 2025, *MNRAS Letters*, 541, L37
- Sommerhagen V., Mannucci F., Cresci G., Maiolino R., Marconi A., Nagao T., Baroni A., Grazian A., 2012, *A&A*, 539, A136
- Speagle J. S., 2020, *MNRAS*, 493, 3132
- Stanton T. M. et al., 2024, *MNRAS*, 532, 3102
- Stanton T. M. et al., 2025, *MNRAS*, 537, 1735
- Stanway E. R., Eldridge J. J., 2018, *MNRAS*, 479, 75
- Stanway E. R., Eldridge J. J., Becker G. D., 2016, *MNRAS*, 456, 485
- Steffen M., Prakatavičius D., Caffau E., Ludwig H. G., Bonifacio P., Cayrel R., Kučinskas A., Livingston W. C., 2015, *A&A*, 583, A57
- Steidel C. C. et al., 2014, *ApJ*, 795, 165
- Steidel C. C., Erb D. K., Shapley A. E., Pettini M., Reddy N., Bogosavljević M., Rudie G. C., Rakic O., 2010, *ApJ*, 717, 289
- Steidel C. C., Shapley A. E., Pettini M., Adelberger K. L., Erb D. K., Reddy N. A., Hunt M. P., 2004, *ApJ*, 604, 534
- Steidel C. C., Strom A. L., Pettini M., Rudie G. C., Reddy N. A., Trainor R. F., 2016, *ApJ*, 826, 159
- Strom A. L., Rudie G. C., Steidel C. C., Trainor R. F., 2022, *ApJ*, 925, 116
- Strom A. L., Steidel C. C., Rudie G. C., Trainor R. F., Pettini M., 2018, *ApJ*, 868, 117
- Strom A. L., Steidel C. C., Rudie G. C., Trainor R. F., Pettini M., Reddy N. A., 2017, *ApJ*, 836, 164
- Sybilka A., Kuntschner H., van de Ven G., Vazdekis A., Falcón-Barroso J., Peletier R. F., Lisker T., 2018, *MNRAS*, 476, 4501
- Tamm A., Tempel E., Tenjes P., Tihhonova O., Tuvikene T., 2012, *A&A*, 546, A4
- Tan V. Y. Y. et al., 2024, preprint (arXiv:2412.07829)
- Tinsley B. M., 1979, *ApJ*, 229, 1046
- Tolstoy E., Hill V., Tosi M., 2009, *ARA&A*, 47, 371
- Topping M. W., Shapley A. E., Reddy N. A., Sanders R. L., Coil A. L., Kriek M., Mobasher B., Siana B., 2020a, *MNRAS*, 495, 4430
- Topping M. W., Shapley A. E., Reddy N. A., Sanders R. L., Coil A. L., Kriek M., Mobasher B., Siana B., 2020b, *MNRAS*, 499, 1652
- Toribio San Cipriano L., Domínguez-Guzmán G., Esteban C., García-Rojas J., Mesa-Delgado A., Bresolin F., Rodríguez M., Simón-Díaz S., 2017, *MNRAS*, 467, 3759
- Tsakonas C., Arnaboldi M., Bhattacharya S., Hammer F., Yang Y., Gerhard O., Wyse R. F. G., Hatzidimitriou D., 2025, *A&A*, 699, 24
- Tsamis Y. G., Barlow M. J., Liu X. W., Danziger I. J., Storey P. J., 2003, *MNRAS*, 338, 687
- Valenti J. A., Piskunov N., 1996, *A&AS*, 118, 595
- Van der Swaelmen M., Hill V., Primas F., Cole A. A., 2013, *A&A*, 560, A44
- VandenBerg D. A., Brogaard K., Leaman R., Casagrande L., 2013, *ApJ*, 775, 134
- Vasiliev E., Belokurov V., Erkal D., 2021, *MNRAS*, 501, 2279
- Veilleux S., Osterbrock D. E., 1987, *ApJS*, 63, 295
- Velichko A., De Cia A., Konstantopoulou C., Ledoux C., Krogager J.-K., Ramburuth-Hurt T., 2024, *A&A*, 685, A103

- Venn K. A., Irwin M., Shetrone M. D., Tout C. A., Hill V., Tolstoy E., 2004, *AJ*, 128, 1177
- Vincenzo F., Kobayashi C., Taylor P., 2018, *MNRAS*, 480, L38
- Virtanen P. et al., 2020, *Nat. Methods*, 17, 261
- Viswanathan A., Horta D., Price-Whelan A. M., Starkenburg E., 2024, preprint ([arXiv:2411.12165](https://arxiv.org/abs/2411.12165))
- Wallerstein G., 1962, *ApJS*, 6, 407
- Wetzel A. R., Hopkins P. F., Kim J.-h., Faucher-Giguère C.-A., Kereš D., Quataert E., 2016, *ApJ*, 827, L23
- Wisnioski E. et al., 2015, *ApJ*, 799, 209
- Woosley S. E., Heger A., Weaver T. A., 2002, *Rev. Mod. Phys.*, 74, 1015
- Woosley S. E., Weaver T. A., 1995, *ApJS*, 101, 181
- Xiang M., Rix H.-W., 2022, *Nature*, 603, 599
- Youakim K. et al., 2020, *MNRAS*, 492, 4986
- Zhang H. et al., 2025, *ApJ*, 983, L10

This paper has been typeset from a \LaTeX file prepared by the author.